High-resolution shock capturing method for simulation of compressible flows

Qijie Li[a,*], Kensuke Yokoi[a,*], Zhihua Xie[a], Syazana Omar[a], Jingjing Xue[a]

[a]*School of Engineering, Cardiff University, Cardiff, CF24 3AA, United Kingdom*

Abstract

Firstly, a new reconstruction strategy is proposed to improve the accuracy of the fifth-order Weighted Essentially Non-Oscillatory (WENO) scheme. It has been noted that conventional WENO schemes still suffer from excessive numerical dissipation near critical regions. One of the reasons is that they tend to under-use all adjacent smooth sub-stencils thus fail to realize optimal interpolation. Hence in this work, a modified WENO (MWENO) strategy is designed to restore the highest possible order interpolation when three target sub-stencils or two target adjacent sub-stencils are smooth. Since the new detector is formulated under the original smoothness indicators, no obvious complexity and cost are added to the simulation. This idea has been successfully implemented into two classical fifth-order WENO schemes, which improve the accuracy near the critical region but without destroying essentially non-oscillatory properties. Secondly, the Tangent of Hyperbola for INterface Capturing (THINC) scheme is introduced as another reconstruction candidate to better represent the discontinuity. Finally, the MWENO and THINC schemes are implemented with the Boundary Variation Diminishing (BVD) algorithm to further minimize the numerical dissipation across discontinuities. Numerical verifications show that the proposed scheme accurately capture both smooth and discontinuous flow structures simultaneously with high-resolution quality. Meanwhile, the presented scheme effectively reduce numerical dissipation error and suppress spurious numerical oscillation in the presence of strong shock or discontinuity for compressible flows and compressible two-phase flows.

Keywords: shock capturing method, boundary variation diminishing scheme, finite volume method, compressible flows, compressible two-phase flows

1. Introduction

A compressible flow is where the fluid compressibility effect cannot be ignored and may even dominate the flow phenomena. For compressible flows, Mach number is significantly bigger than zero and the flow velocity approaches or is larger than the local speed of sound. Most real-case compressible flow problems [8, 11, 60, 29, 41] involve complex flow structures including shock waves and vortices, such as those found in aerodynamics regarding the design of high-speed vehicles [44, 15], gas turbines [46, 33, 37, 59, 16], reciprocating engines [2, 21], combustion engines [56, 47], and jet engines [5]. When compressible flow problems contain a mixing region of two materials with a moving interface, the material interface of compressible two-phase flows make the physics more complicated. For

---

*Corresponding author

Email addresses: `liqijie_kimi@outlook.com` (Qijie Li), `Kensuke.Yokoi@cardiff.ac.uk` (Kensuke Yokoi)

example, shock/interface interactions are thought to be crucial to the instability and evolution of material interfaces that separate different fluids. Compressible two-phase flows are widely found in a wide spectrum of phenomena, e.g. cavitation [13, 26, 38, 35, 57, 40, 7, 4]. Driven by the great demand of these engineering applications, the study and understanding of the physics behind compressible fluid dynamics is crucial.

High-order accurate shock capturing methods are extensively used to simulate compressible flows that involve both complex smooth structures and shocks. The development of this type of advanced numerical method is a long-standing topic of the computational fluid dynamic research field. The difficulties in designing such schemes arise from two points. Firstly, shock capturing schemes should have high enough resolution to solve wide spectral waves. Secondly, numerical schemes should be able to capture discontinuities without obvious numerical oscillations.

One typical high-order numerical scheme is the Essentially Non-Oscillatory (ENO) [20] scheme. The ENO scheme is an essentially non-oscillatory piecewise polynomial reconstruction, which is an extension of the second-order Monotonic Upstream-centered Scheme for Conservation Laws (MUSCL) to an arbitrary order of accuracy. This type of reconstruction algorithm implements an adaptive stencil with piecewise data. With this technique, it can achieve second-order accuracy wherever the region is smooth whilst avoiding Gibbs phenomenon at discontinuities. In classical ENO scheme, a hierarchy reconstruction algorithm is used to determine the local stencil. This reconstruction can be of uniformly high-order accuracy right up to the discontinuity. The drawback of the classical ENO scheme in the stencil choosing process is that $2k - 1$ cells need to be considered in order to build k-th order accuracy in the smooth region. Meanwhile, in the smooth region, the absolute value of the Newton divided difference of both sides candidates are near zero, thus a small change of the round off level would change the selection direction [45]. In this situation, the single side selection is not efficient and may cause the loss of accuracy when it is applied to solve the partial differential equation.

Following the ENO idea, weighted ENO (WENO) schemes [34, 9, 30, 18, 65, 27, 6, 22, 24, 66, 42, 10, 23, 25] were developed. Instead of using only one of the candidates to build the reconstruction, WENO schemes use a combination of all candidate stencils. In 1994, Liu et al. proposed the first version of WENO schemes [34] to solve the one-dimensional conservation laws. An efficient implementation of the WENO scheme was proposed by Jiang and Shu (WENO-JS) [27]. Although WENO-JS scheme achieves high accuracy in smooth part, the convergence decreases at critical points. To increase the convergence rate at critical points, the mapping function was introduced in WENO scheme [22] to map the set of weights. However, the mapping processes increase the computation cost. Without increasing CPU time significantly, an improved weighted essentially non-oscillatory scheme of Borges (WENO-Z)[6] was proposed to increase the accuracy near critical points. In WENO-Z scheme, a high-order smoothness indicator is devised as a linear combination of the lower order local smoothness indicators. New non-oscillatory weights are built to achieve optimal order near critical points. Numerical dissipation can be reduced by assigning large weights to non-smooth stencils. In addition, some adaptive and hybrid WENO schemes [30, 18, 10] are proposed to improve the resolution at critical regions. To achieve both high-order and nonlinear adaption, an adaptive central-upwind WENO (WENO-CU) scheme was proposed by Hu et al. [24]. A family of targeted ENO (TENO) schemes were proposed in [14] to achieve low numerical dissipation by introducing a cutoff function to renormalize the optimal weights.

Compared with the classical WENO scheme which assigns smooth weights to candidate stencils, TENO schemes can eliminate a candidate stencil entirely when it contains a genuine discontinuity with a certain strength. The above works indicate that nonlinear weights in WENO schemes are one of the main sources of numerical dissipation. In the smooth region, the value of nonlinear weights should recover their optimal linear weights. In the discontinuous region, the weights for stencils containing discontinuities are assigned with small values. However, in this case, the weights for other smooth stencils are not guaranteed to recover their optimal ones.

Recently, the Boundary Variation Diminishing (BVD) [54, 12] algorithm was proposed as a novel guideline for constructing high-fidelity shock capturing methods. The original BVD algorithm was designed for finite volume method based on WENO-Z and Tangent of Hyperbola for INterface Capturing (THINC) schemes. This reconstruction approach effectively reduce numerical dissipation in Riemann solver by minimising the variations of the reconstruction values at cell boundaries. In the BVD reconstruction algorithm, two candidate schemes are used to construct the interpolation functions. In order to enable the resulting scheme to accurately solve both smooth and discontinuous solutions, a high-order polynomial function (e.g. WENO-Z [6]) is used for the smooth solution and a sigmoid function (e.g. THINC [63, 64]) is used for the discontinuous solution. The superior performance of BVD reconstruction indicates that the great potential of designing novel numerical methods with better properies based on the BVD principle.

In the present work, we implement the BVD reconstruction strategy using MWENO schemes and THINC method. The reconstruction criterion of BVD-MWENO-THINC schemes are designed by the boundary variation diminishing algorithm. With this implementation, the accuracy near the critical region can be improved without destroying essentially non-oscillatory properties and numerical dissipation can be effectively reduced.

This paper is organized as follows: In Section 2, firstly, the numerical methodology of the fifth-order WENO-JS [27] and WENO-Z [6] schemes are given as a general introduction. Secondly, the reconstruction strategy of the modofied WENO (MWENO) scheme is described. After that, the THINC scheme is explained. Based on the Modified WENO idea and THINC method, we present the BVD-MWENOJS-THINC and BVD-MWENOZ-THINC schemes by implementing the total boundary variation diminishing algorithm to select an appropriate reconstruction scheme. In Section 3, several types of benchmark tests are carried out to validate the capability of the proposed scheme by solving linear advection equation, Euler equations, and compressible two phase flow problem. Finally, we summarize the paper with some conclusions in Section 4.

2. Numerical methods

2.1. Governing equations of compressible flows

The features of inviscid compressible fluid dynamics [58] can be mathematically described by the following Euler equations

$$\frac{\partial \rho}{\partial t} + \nabla \cdot \mathbf{m} = 0, \tag{1}$$

$$\frac{\partial \mathbf{m}}{\partial t} + \nabla \cdot (\mathbf{m} \otimes \mathbf{u} + p\boldsymbol{\delta}) = 0, \tag{2}$$

3

$$\frac{\partial E}{\partial t} + \nabla \cdot (\mathbf{u}E + \mathbf{u}p) = 0, \tag{3}$$

where ρ is density, $\mathbf{u} = (u, v, w)$ is velocity, $\mathbf{m} = (m_x, m_y, m_z)$ is momentum, p is pressure, and E is total energy.

2.1.1. Reconstruction method

For the sake of simplicity, the numerical method is explained in one dimension. It can be directly extended to the multi-dimensions on structured grids in dimension-wise reconstruction fashion. We consider the following hyperbolic conservation law

$$\frac{\partial u}{\partial t} + \frac{\partial f(u)}{\partial x} = 0, \tag{4}$$

where u is the solution function and $f(u)$ is the flux function. In this paper, the mesh is assumed to be uniform, the cell centers are defined as $x_i = i\Delta x$ and the cell boundaries are given by $x_{i+1/2} = x_i + \frac{1}{2}\Delta x$, where $\Delta x = x_{i+1/2} - x_{i-1/2}$.

In finite volume methods, the cell average value for cell I_i is defined as

$$\bar{u}_i = \frac{1}{\Delta x} \int_{x_{i-1/2}}^{x_{i+1/2}} u(x,t)dx. \tag{5}$$

$\bar{u}_i$ is updated by

$$\frac{d\bar{u}_i}{dt} = -\frac{1}{\Delta x}(f_{i+1/2} - f_{i-1/2}). \tag{6}$$

The numerical fluxs $f_{i+1/2}$ and $f_{i-1/2}$ are calculated by a Riemann solver. In spite of different variants, the canonical form of the Riemann flux can be written as

$$f_{i+1/2}^{Riemann}(u_{i+1/2}^L, u_{i+1/2}^R) = \frac{1}{2}\left(f(u_{i+1/2}^L) + f(u_{i+1/2}^R) - |\alpha_{i+1/2}|(u_{i+1/2}^R - u_{i+1/2}^L)\right), \tag{7}$$

where $\alpha_{i+1/2}$ is the characteristic speed in a hyperbolic equation. $u_{i+1/2}^L$ and $u_{i+1/2}^R$ are the left-side value and right-side value for cell boundaries $u_{i+1/2}^L$ at $x_{i+1/2}, i = 1, 2, ..., N$. In this paper, Roe's approximate Riemann solver [58] is used to compute the numerical fluxes. To obtain solutions of the Riemann solver, a core problem is how to reconstruct the left- and right-side values for cell boundaries, which can fundamentally influence the numerical solution.

2.1.2. Review of the fifth-order WENO-JS and WENO-Z schemes

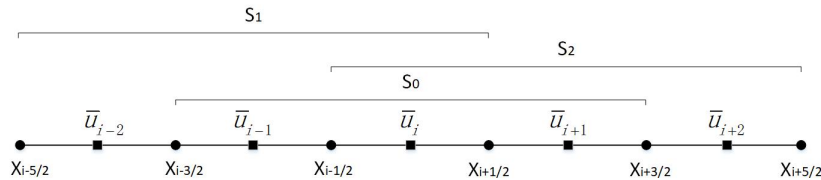Figure 1: Sketch of the fifth-order WENO reconstruction on the computational uniform grid. The candidate stencils include three 3-cells sub-stencils S_0, S_1, S_2 .

In the conventional fifth-order WENO scheme, three polynomials constructed over stencils $S_0, S_1,$ and S_2 in Fig. 1 are used to compute $u_{i+1/2}^L$ as

$$u_{i+1/2}^L = \omega_0 u_{i+1/2}^{S_0} + \omega_1 u_{i+1/2}^{S_1} + \omega_2 u_{i+1/2}^{S_2}, \tag{8}$$

where $u_{i+1/2}^{S_0}, u_{i+1/2}^{S_1}, u_{i+1/2}^{S_2}$ are calculated by

$$u_{i+1/2}^{S_0} = -\frac{1}{6}\bar{u}_{i-1} + \frac{5}{6}\bar{u}_i + \frac{1}{3}\bar{u}_{i+1}, \tag{9}$$

$$u_{i+1/2}^{S_1} = \frac{1}{3}\bar{u}_{i-2} - \frac{7}{6}\bar{u}_{i-1} + \frac{11}{6}\bar{u}_i, \tag{10}$$

$$u_{i+1/2}^{S_2} = \frac{1}{3}\bar{u}_i + \frac{5}{6}\bar{u}_{i+1} - \frac{1}{6}\bar{u}_{i+2}. \tag{11}$$

Nonlinear weights ω_k can be calculated with different formulations. In the WENO-JS scheme [27], ω_k are defined as

$$\omega_k = \frac{\alpha_k}{\sum_{k=0}^{k=2}\alpha_k}, \alpha_k = \frac{d_k}{(\beta_i^k + \varepsilon)^p}, k = 0, 1, 2. \tag{12}$$

Here the linear paramaters $d_0 = 0.6$, $d_1 = 0.1$ and $d_2 = 0.3$. ε is a small value to prevent division by zero. Generally, $p = 2$ is used in the WENO-JS scheme to accelerate the nonlinear adaptation towards the essentially non-oscillatory property. The local smoothness indicator [27] is defined by

$$\beta_i^k = \sum_{l=1}^{2} \Delta x^{2l-1} \int_{x_{i-1/2}}^{x_{i+1/2}} \left(\frac{d^l}{dx^l}u_i^k(x)\right)^2 dx. \tag{13}$$

In FVM, based on cell-averaged values $\bar{u}_i$, the explicit form of smoothness indicator β_i^k can be expressed as follows

$$\begin{cases} \beta_0 = \frac{13}{12}(\bar{u}_{i-1} - 2\bar{u}_i + \bar{u}_{i+1})^2 + \frac{1}{4}(\bar{u}_{i-1} - \bar{u}_{i+1})^2, \\ \beta_1 = \frac{13}{12}(\bar{u}_{i-2} - 2\bar{u}_{i-1} + \bar{u}_i)^2 + \frac{1}{4}(\bar{u}_{i-2} - 4\bar{u}_{i-1} + 3\bar{u}_i)^2, \\ \beta_2 = \frac{13}{12}(\bar{u}_i - 2\bar{u}_{i+1} + \bar{u}_{i+2})^2 + \frac{1}{4}(3\bar{u}_i - 4\bar{u}_{i+1} + \bar{u}_{i+2})^2. \end{cases} \tag{14}$$

To improve the behavior of non-linear weights of WENO scheme, another weighting strategy for α_k is proposed in the WENO-Z scheme [6] as

$$\alpha_k = d_k\left(1 + \left(\frac{\tau_0}{\beta_k + \varepsilon}\right)^p\right), \tau_0 = |\beta_2 - \beta_1|. \tag{15}$$

where d_k, β_i^k and ε are same with the WENO-JS scheme, while $p = 1$ is suggested to control the excessive numerical dissipation in non-smooth regions. Although WENO-Z scheme improves the accuracy than the original WENO scheme, it does not recover the possible highest order in the vicinity of critical points where high order derivatives and fine smooth structure may be treated as discontinuity and contributions of the polynomials over different candidate stencils are not optimized.

2.1.3. Modified WENO (MWENO) schemes

In this section, we propose a variant of the fifth-order WENO scheme. Unlike the conventional fifth-order WENO scheme, e.g. WENO-JS and WENO-Z, MWENO restores the highest possible order interpolation when three target sub-stencils or two adjacent target sub-stencils are smooth. MWENO is based on the three reconstructin candidates $u_{i+1/2}^{S_0}, u_{i+1/2}^{S_1}, u_{i+1/2}^{S_2}$ as in Eqs. (9), (10), and (11). A detector is proposed to indicate the smoothness and the potential location of the discontinuity. This detector is formulated based on the original smoothness indicators $\beta_i^k (k = 1, 2, 3)$

and τ_0 in the WENOZ scheme. In addition to the τ_0 defined in Eq. (12), τ_1 and τ_2 [48] are introduced to design the detector, and they can be computed by

$$
\begin{cases}
\tau_1 = |\beta_i^0 - \beta_i^1|, \\
\tau_2 = |\beta_i^0 - \beta_i^2|.
\end{cases}
\tag{16}
$$

The reconstruction criterion and the detector are designed as follows

- Case 1. If the entire reconstruction region between $x_{i-5/2}$ and $x_{i+5/2}$ is continuous, three smooth sub-stencils S_0, S_1, and S_2 in Fig. 1 are targeted and selected. To identify case 1, Taylor series expansions of τ_k and $\beta_i^k (k=1,2,3)$ at x_i are used as follows

$$
\begin{cases}
\beta_i^0 = u_i'^2 \Delta x^2 + (\frac{13}{12} u_i''^2 + \frac{1}{3} u_i' u_i''') \Delta x^4 + O(\Delta x^6), \\
\beta_i^1 = u_i'^2 \Delta x^2 + (\frac{13}{12} u_i''^2 - \frac{2}{3} u_i' u_i''') \Delta x^4 - (\frac{13}{6} u_i'' u_i''' - \frac{1}{2} u_i' u_i'''') \Delta x^5 + O(\Delta x^6), \\
\beta_i^2 = u_i'^2 \Delta x^2 + (\frac{13}{12} u_i''^2 - \frac{2}{3} u_i' u_i''') \Delta x^4 + (\frac{13}{6} u_i'' u_i''' - \frac{1}{2} u_i' u_i'''') \Delta x^5 + O(\Delta x^6),
\end{cases}
\tag{17}
$$

$$
\begin{cases}
\tau_0 = |(\frac{13}{3} u_i'' u_i''' - u_i' u_i'''') \Delta x^5| + O(\Delta x^6), \\
\tau_1 = |(u_i' u_i''') \Delta x^4 + (\frac{13}{6} u_i'' u_i''' - \frac{1}{2} u_i' u_i'''') \Delta x^5| + O(\Delta x^6), \\
\tau_2 = |(u_i' u_i''') \Delta x^4 - (\frac{13}{6} u_i'' u_i''' - \frac{1}{2} u_i' u_i'''') \Delta x^5| + O(\Delta x^6).
\end{cases}
\tag{18}
$$

As demonstrated by Rafael et al. [6], if the entire stencil does not contain discontinuities, then $\tau_0(\Delta x^5) << \beta_i^{\hat{j}}(\Delta x^2)$. The indicator is designed as $\tau_0 \leq min(\beta_i^0, \beta_i^1, \beta_i^2)$. In this case, the reconstruction is based on $u_{i+1/2}^{S_0}$, $u_{i+1/2}^{S_1}$, and $u_{i+1/2}^{S_2}$, which are assigned with the optimal linear weights as

$$
u_{i+1/2}^L = \frac{6}{10} u_{i+1/2}^{S_0} + \frac{1}{10} u_{i+1/2}^{S_1} + \frac{3}{10} u_{i+1/2}^{S_2}
\tag{19}
$$

- Case 2. If the discontinuity exists in the region between $x_{i-5/2}$ and $x_{i-3/2}$, as shown in Fig. 2, it suggests that
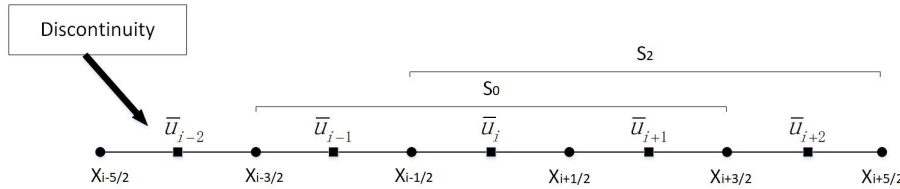

Figure 2: Discontinuity exists in sub-stencil S_1, while adjacent sub-stencils S_0 and S_2 are smooth.

the reconstruction solution is continuous in stencils S_0 and S_2, $\tau_2 \leq min(\beta_i^0, \beta_i^1, \beta_i^2)$. In addition, the solution is discontinious on stencil S_1, $\beta_i^1 >> \beta_i^0$ and $\beta_i^1 >> \beta_i^2$, $\tau_1 = |\beta_i^0 - \beta_i^1| > \beta_i^0$ and $\tau_1 > \beta_i^2$. The indicator is designed as $\tau_0 > min(\beta_i^0, \beta_i^1, \beta_i^2)$, $\tau_1 > min(\beta_i^0, \beta_i^1, \beta_i^2)$, and $\tau_2 \leq min(\beta_i^0, \beta_i^1, \beta_i^2)$. In this case, two smooth adjacent sub-stencils S_0 and S_2 are targeted and selected, the reconstruction is based on $u_{i+1/2}^{S_0}$ and $u_{i+1/2}^{S_2}$, which are assigned with the optimal linear weights as

$$
u_{i+1/2}^L = \frac{1}{2} u_{i+1/2}^{S_0} + \frac{1}{2} u_{i+1/2}^{S_2}.
\tag{20}
$$

6

- Case 3. Analogously, if the discontinuity appears in the region between $x_{i+3/2}$ and $x_{i+5/2}$, as shown in Fig. 3, it suggests that the reconstruction solution is continuous in stencils S_0 and S_1, but discontinuous in stencil S_2. The detector is designed as $\tau_0 > min(\beta_i^0, \beta_i^1, \beta_i^2)$, $\tau_2 > min(\beta_i^0, \beta_i^1, \beta_i^2)$, and $\tau_1 \leq min(\beta_i^0, \beta_i^1, \beta_i^2)$. In this case, two smooth adjacent sub-stencils S_0 and S_1 are targeted and selected, and the reconstruction is based on $u_{i+1/2}^{S_0}$ and $u_{i+1/2}^{S_1}$ are assigned with the optimal linear weights as

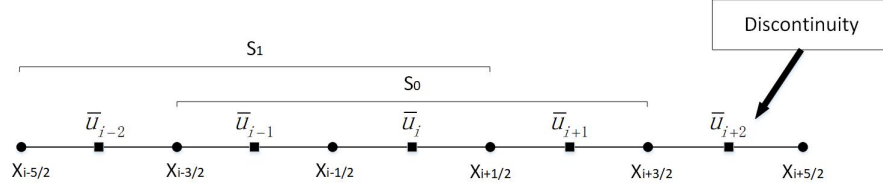$$u_{i+1/2}^L = \frac{3}{4}u_{i+1/2}^{S_0} + \frac{1}{4}u_{i+1/2}^{S_1}. \tag{21}$$

Figure 3: Discontinuity exists in sub-stencil S_2, while adjacent sub-stencils S_0 and S_1 are smooth.

- Case 4. In addition to the above situations, all three sub-stencils S_0, S_1, and S_2 are targeted and selected. The reconstruction is based on $u_{i+1/2}^{S_0}$, $u_{i+1/2}^{S_1}$, and $u_{i+1/2}^{S_2}$, which are assigned with the non-linear weights as

$$u_{i+1/2}^L = \omega_0 u_i^{S_0}(x_{i+1/2}) + \omega_1 u_i^{S_1}(x_{i+1/2}) + \omega_2 u_i^{S_2}(x_{i+1/2}). \tag{22}$$

The non-linear weights ω_k can be calculated by using either WNENO-JS or WENO-Z.

In summary, the construction criterion of MWENO scheme can be expressed as follws

$$\phi_{i+1/2}^L = \begin{cases} \frac{6}{10}\phi_{i+1/2}^{S_0} + \frac{1}{10}\phi_{i+1/2}^{S_1} + \frac{3}{10}\phi_{i+1/2}^{S_2} & \text{if } \tau_0 \leq min(\beta_i^0, \beta_i^1, \beta_i^2) \\ \frac{1}{2}\phi_{i+1/2}^{S_0} + \frac{1}{2}\phi_{i+1/2}^{S_2} & \text{if } \tau_0 > min(\beta_i^0, \beta_i^1, \beta_i^2), \tau_1 > min(\beta_i^0, \beta_i^1, \beta_i^2), \text{ and } \tau_2 \leq min(\beta_i^0, \beta_i^1, \beta_i^2), \\ \frac{3}{4}\phi_{i+1/2}^{S_0} + \frac{1}{4}\phi_{i+1/2}^{S_1} & \text{else if } \tau_0 > min(\beta_i^0, \beta_i^1, \beta_i^2), \tau_2 > min(\beta_i^0, \beta_i^1, \beta_i^2), \text{ and } \tau_1 \leq min(\beta_i^0, \beta_i^1, \beta_i^2) \\ \omega_i^0\phi_{i+1/2}^{S_0} + \omega_i^1\phi_{i+1/2}^{S_1} + \omega_i^2\phi_{i+1/2}^{S_2} & \text{else .} \end{cases} \tag{23}$$

2.1.4. THINC scheme

Unlike WENO method, the tangent of hyperbola for interface capturing (THINC) [63, 64] scheme is a jump-like reconstruction with a differentiable and monotone function, which can be defined as

$$u_i^{THINC}(x) = u_{min} + \frac{u_{max}}{2}\left(1 + \gamma tanh\left(\beta^T\left(\frac{x - x_{i-1/2}}{x_{i+1/2} - x_{i-1/2}} - \tilde{x}\right)\right)\right), \tag{24}$$

where $u_{min} = min(\bar{u}_{i-1}, \bar{u}_{i+1})$, $u_{max} = max(\bar{u}_{i-1}, \bar{u}_{i+1})$, $\gamma = sgn(\bar{u}_{i+1} - \bar{u}_{i-1})$, and the location of the jump center $\tilde{x}$ is computed from the constraint condition of Eq. 5. β^T is a prescribed parameter. The explicit expression for the THINC reconstruction of the left-side value $u_{i+1/2}^L$ for cell boundaries $x_{i+1/2}$ can be given as

$$u_{i+1/2}^L = u_i^{THINC}(x_{i+1/2}) = u_{min} + \frac{\phi_{max}}{2}\left(1 + \gamma\frac{tanh(\beta^T) + A}{1 + Atanh(\beta^T)}\right), \tag{25}$$

where $A = \frac{B/\cosh(\beta^T)-1}{\tanh(\beta^T)}$, $B = exp(\gamma\beta^T(2C-1))$, $C = \frac{\bar{u}_i - \bar{u}_{min} + \varepsilon}{u_{max} + \varepsilon}$, and $\varepsilon = 10^{-20}$. Compared with the polynomial functions used in WENO schemes, THINC can represent the discontinuity with less numerical errors.

2.1.5. Boundary variation diminishing(BVD) reconstruction

Based on the proposed modified WENO schemes and THINC scheme, a total Boundary Variation Diminishing (BVD) algorithm [54] is implemented to further minimize the numerical dissipation across discontinuities. To explain the concept of this BVD selection process, we define $u_{i-1}^{MWENO,L}(x_{i-1/2})$ and $u_i^{MWENO,R}(x_{i-1/2})$ to represent the MWENO reconstruction of the left-side value $u_{i-1/2}^L$ and the right-side value $u_{i-1/2}^R$ for cell boundaries $x_{i-1/2}, i = 1,2,...N$. Analogously, we use $u_{i-1}^{THINC,L}(x_{i-1/2})$ and $u_i^{THINC,R}(x_{i-1/2})$ to represent the THINC reconstruction of the left-side value $u_{i-1/2}^L$ and the right-side value $u_{i-1/2}^R$ for cell boundaries. The total boundary variation (TBV) for the MWENO reconstruction and the THINC reconstruction at the boundaries of each cell are defined as

$$
\begin{cases}
TBV_i^{MWENO} = |u_i^{MWENO,R}(x_{i-1/2}) - u_{i-1}^{MWENO,L}(x_{i-1/2})| + |u_i^{MWENO,L}(x_{i+1/2}) - u_{i+1}^{MWENO,R}(x_{i+1/2})|, \\
TBV_i^{THINC} = |u_i^{THINC,R}(x_{i-1/2}) - u_{i-1}^{THINC,L}(x_{i-1/2})| + |u_i^{THINC,L}(x_{i+1/2}) - u_{i+1}^{THINC,R}(x_{i+1/2})|.
\end{cases}
\tag{26}
$$

If $TBV_i^{THINC} < TBV_i^{MWENO}$, the total boundary variation for the target cell of the THINC reconstruction is smaller than that of the MWENO reconstruction. In this case, discontinuity may exist, and THINC is selected to minimise the TBV. Otherwise, MWENO is selected to keep the high-order reconstruction for smooth solutions.

In summary, the reconstruction criterion of the BVD-MWENO-THINC scheme for the left-side value $u_{i+1/2}^L$ can be expressed as follow

$$
u_{i+1/2}^L =
\begin{cases}
u_i^{THINC,L}(x_{1+1/2}) & \text{if } TBV_i^{THINC} < TBV_i^{MWENO}, \\
u_i^{MWENO,L}(x_{1+1/2}) & \text{else}
\end{cases}
\tag{27}
$$

Analogously, we can get the right-side value $u_{i+1/2}^R$.

2.2. Time evolution method

In terms of time discretization method, third-order Runge-Kutta[17] method is used for time advancing, which is given by

$$
\begin{aligned}
u_j^{(1)} &= u_j^n + \Delta t F(u_j^n), \\
u_j^{(2)} &= \tfrac{3}{4}u_j^n + \tfrac{1}{4}u_j^{(1)} + \tfrac{1}{4}\Delta t F(u_j^{(1)}), \\
u_j^{(n+1)} &= \tfrac{1}{3}u_j^n + \tfrac{2}{3}u_j^{(2)} + \tfrac{2}{3}\Delta t F(u_j^{(2)}).
\end{aligned}
\tag{28}
$$

where $u_j^{(1)}$ and $u_j^{(2)}$ denote the intermediate values at the sub-steps.

3. Numerical results

In this section, spectral property analysis of the proposed modified WENO schemes is given compared to WENO-JS and WENO-Z schemes. Benchmark tests of linear and non-linear advection equations and Euler equations are solved to verify the proposed schemes. Firstly, linear advection tests are conducted to demonstrate the performance of the proposed modified WENO schemes and BVD implementations. Secondly, several Euler tests are used to further show

the superior performance of the proposed BVD-MWENOZ-THINC scheme compared WENOZ and BVD-MWENO-THINC schemes in the simulation of compressible single phase problems. Lastly, the proposed BVD-MWENOZ-THIHC scheme is extended to solve the five-equation model for compressible two-phase flow problems. When solving Euler equations, an approximate Riemann solver Harten Lax and van Leer Contact (HLLC) [58] is used for calculating numerical fluxes.

3.1. Analysis of spectral property

In this part, the spectral property of the proposed modified WENO schemes are verified by using the approximate dispersion relation method[39], which evaluates the numerical dissipation and dispersion of a scheme from the real and imaginary parts of the modified wavenumber.
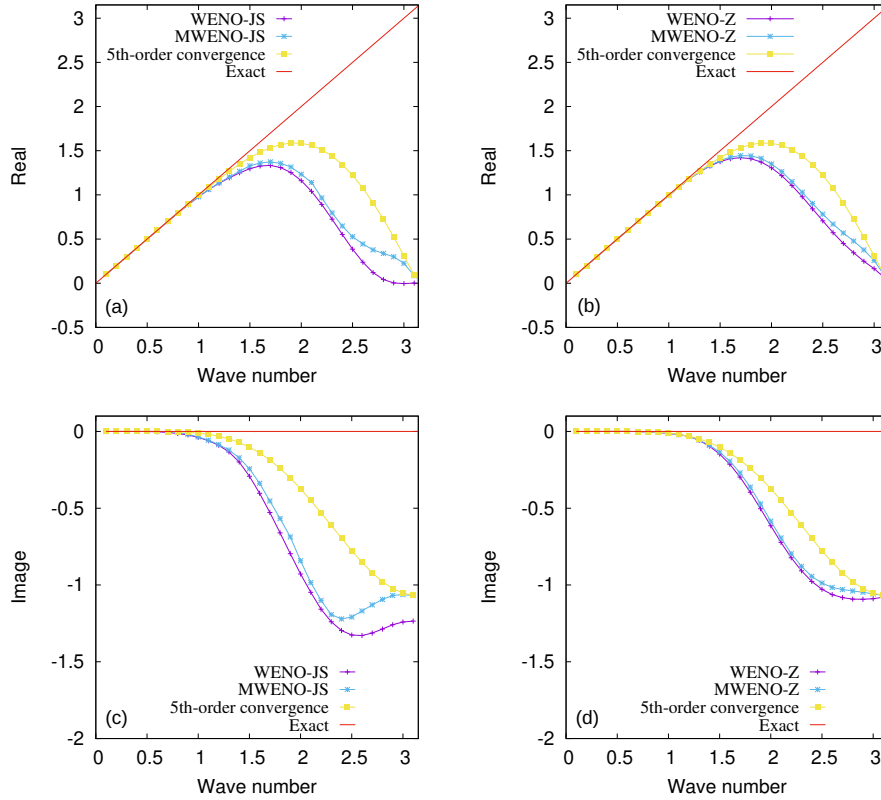

Figure 4: Approximate dispersion and dissipation properitiesfor WENO-JS, WENO-Z, MWENO-JS, MWENO-Z and 5th Upwind schemes. Real parts and imaginary parts of modified wavenumber are shown are shown in (a), (b) and (c), (d), respectively.

Spectral properties of WENO-JS, WENO-Z, MWENO-JS, and MWENO-Z schemes with different wave number are illustrated in Fig. 4. It is observed that WENO-JS and WENO-Z have discrepancies compared to MWENO-JS and MWENO-Z in the higher wavenumber region due to the reason that these WENO smoothness indicators tend to mis-interpret between discontinuities and high wavenumber structures. The proposed modified WENO approach maintains non-oscillation property and enables to improve the performance of spectral property in the high-wavenumber region.

3.2. Analysis of smooth profile containing critical points advection

Spectral properties analysis has shown the superior performance of the proposed modified WENO schemes. To further demonstrate their performance for critical region, an advection of a smooth profile containing critical points is used in this part. The initial condition is $\phi(x,0) = \sin^4(\pi x), -1 \leq x \leq 1$, which contains critical points where high order derivative does not simultaneously vanish [27]. The definition of L_1 and L_∞ are defined as follows

$$L_1 = \frac{1}{N} \sum_{i=1}^{N} |\phi_i - \phi_{exact,i}|, \tag{29}$$

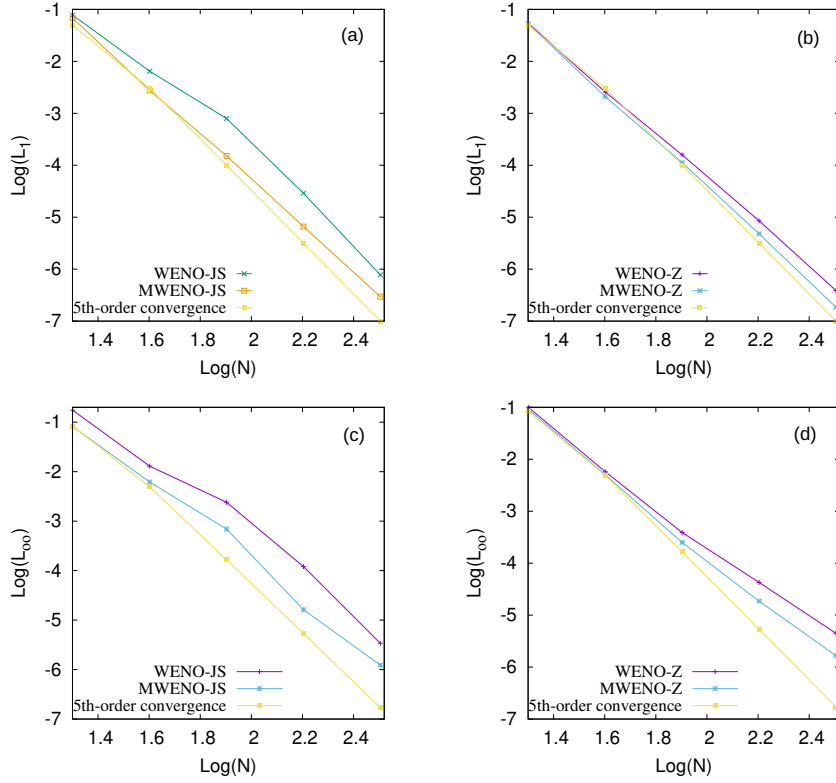$$L_\infty = \max(|\phi_i - \phi_{exact,i}|). \tag{30}$$

Figure 5: Numerical errors L_1 and L_∞ as a function of the number of grid cells are shown in (a), (b) and (c), (d), respectively. Comparisons are made among WENO-JS, WENO-Z and the proposed MWENO-JS and MWENO-Z schemes.

Fig. 5 shows numerical results of WENO-JS, WENO-Z, MWENO-JS, MWENO-Z schemes for calculating L_1 and L_∞ errors. It is observed that conventional WENO schemes do not reach their formal order of accuracy at critical points [22]. WENO-JS and WENO-Z schemes lose accuracy as the number of grid cells increase. However, both MWENO-JS and MWENO-Z schemes improve the accuracy with refined meshes. This is because that WENO-JS and WENO-Z tend to under-use all adjacent smooth sub-stencils thus fail to realize optimal interpolation in the vicinity of critical points. In contrast, MWENO-JS and MWENO-Z are designed to restore the highest possible order interpolation when target sub-stencils are smooth. This indicates that unlike WENO-JS and WENO-Z schemes, the proposed MWENO-JS and MWENO-Z schemes can achieve higher order accuracy even for profiles containing critical points.

3.3. Linear advection equation

Furthermore, we present numerical results of various advection tests by solving the linear advection equation with periodic boundary conditions. The numerical results of the MWENO and BVD-MWENO-THINC schemes are compared with the results of the WENO-Z [6] and BVD-WENOZ-THINC [54] schemes.

3.3.1. Accuracy test for advection of sine wave

This test is used to check the convergence rate of the proposed target WENO schemes and BVD implementations. The smooth initial condition is $\phi(x,0) = \sin(\pi x) + 0.5$. The computation domain is $[0,1]$, $u(x) = 1$ and periodic boundary conditions are used. Four different grid sizes (N = 20, 40, 80, 160 and 320) are used and CFL number is 0.4.

Table 1: Errors and orders of convergence for sine wave propagation test $\phi(x,0) = \sin(\pi x) + 0.5$, at t=2.

Method	N	L_1 error	L_1 order	L_∞ error	L_∞ order
WENO-JS	20	2.11×10^{-3}	-	3.48×10^{-3}	-
	40	6.69×10^{-5}	4.98	1.25×10^{-4}	4.80
	80	2.09×10^{-6}	5.00	4.06×10^{-6}	4.94
	160	6.53×10^{-8}	5.00	1.25×10^{-7}	5.02
	320	2.04×10^{-9}	5.00	3.80×10^{-9}	5.04
WENO-Z	20	3.18×10^{-4}	-	4.99×10^{-4}	-
	40	9.53×10^{-6}	5.06	1.52×10^{-5}	5.04
	80	2.98×10^{-7}	5.00	4.71×10^{-7}	5.01
	160	9.33×10^{-9}	5.00	1.47×10^{-9}	5.00
	320	2.90×10^{-10}	5.01	4.57×10^{-10}	5.01
MWENO-JS	20	2.97×10^{-4}	-	4.65×10^{-4}	-
	40	9.49×10^{-6}	4.97	1.49×10^{-5}	4.96
	80	2.98×10^{-7}	4.99	4.69×10^{-7}	4.99
	160	9.33×10^{-9}	5.00	1.47×10^{-8}	5.00
	320	2.90×10^{-10}	5.01	4.57×10^{-10}	5.01
MWENO-Z	20	2.97×10^{-4}	-	4.65×10^{-4}	-
	40	9.49×10^{-6}	4.97	1.49×10^{-5}	4.96
	80	2.98×10^{-7}	4.99	4.69×10^{-7}	4.99
	160	9.33×10^{-9}	5.00	1.47×10^{-8}	5.00
	320	2.90×10^{-10}	5.01	4.57×10^{-10}	5.01
5th upwind	20	2.97×10^{-4}	-	4.65×10^{-4}	-
	40	9.49×10^{-6}	4.97	1.49×10^{-5}	4.96
	80	2.98×10^{-7}	4.99	4.69×10^{-7}	4.99
	160	9.33×10^{-9}	5.00	1.47×10^{-8}	5.00
	320	2.90×10^{-10}	5.01	4.57×10^{-10}	5.01

Table 2: Errors and orders of convergence for sine wave propagation test $\phi(x,0) = \sin(\pi x) + 0.5$, at t=2.

Method	N	L_1 error	L_1 order	L_∞ error	L_∞ order
BVD-WENOJS-THINC	20	2.11×10^{-3}	-	3.48×10^{-3}	-
	40	6.69×10^{-5}	4.98	1.25×10^{-4}	4.80
	80	2.09×10^{-6}	5.00	4.06×10^{-6}	4.94
	160	6.53×10^{-8}	5.00	1.25×10^{-7}	5.02
	320	2.04×10^{-9}	5.00	3.80×10^{-9}	5.04
BVD-WENOZ-THINC	20	3.18×10^{-4}	-	4.99×10^{-4}	-
	40	9.53×10^{-6}	5.06	1.52×10^{-5}	5.04
	80	2.98×10^{-7}	5.00	4.71×10^{-7}	5.01
	160	9.33×10^{-9}	5.00	1.47×10^{-9}	5.00
	320	2.90×10^{-10}	5.06	4.57×10^{-10}	5.01
BVD-MWENOJS-THINC	20	2.97×10^{-4}	-	4.65×10^{-4}	-
	40	9.49×10^{-6}	4.97	1.49×10^{-5}	4.96
	80	2.98×10^{-7}	4.99	4.69×10^{-7}	4.99
	160	9.33×10^{-9}	5.00	1.47×10^{-8}	5.00
	320	2.90×10^{-10}	5.01	4.57×10^{-10}	5.01
BVD-MWENOZ-THINC	20	2.97×10^{-4}	-	4.65×10^{-4}	-
	40	9.49×10^{-6}	4.97	1.49×10^{-5}	4.96
	80	2.98×10^{-7}	4.99	4.69×10^{-7}	4.99
	160	9.33×10^{-9}	5.00	1.47×10^{-8}	5.00
	320	2.90×10^{-10}	5.01	4.57×10^{-10}	5.01
5th upwind	20	2.97×10^{-4}	-	4.65×10^{-4}	-
	40	9.49×10^{-6}	4.97	1.49×10^{-5}	4.96
	80	2.98×10^{-7}	4.99	4.69×10^{-7}	4.99
	160	9.33×10^{-9}	5.00	1.47×10^{-8}	5.00
	320	2.90×10^{-10}	5.01	4.57×10^{-10}	5.01

Table 1 shows the numerical results of WENO-JS, WENO-Z, MWENO-JS, MWENO-Z, and 5-th order upwind method for one period. We can see that the proposed schemes MWENO-JS, MWENO-Z show an improvement in accuracy over WENO-JS and WENO-Z, and can achieve 5th-order accuracy for the smooth solution. Table 2 shows the numerical results of BVD-WENOJS-THINC, BVD-WENOZ-THINC, BVD-MWENOJS-THINC, and BVD-MWENOZ-THINC, and 5-th order upwind method for one period. It is found that the BVD implementation can automatically choose the high-order reconstruction candidate in the smooth region.

3.3.2. Complex wave propagation test

In this case, we test the proposed scheme through Jiang-Shu complex wave propagation problem [28]. The numerical mesh size is $N = 200$, $\Delta t = 0.4\Delta x$, $\Delta x = 2/N$, $u(x) = 1$, the computational domain is $[-1, 1]$ with the following initial condition

$$
\phi(x,0) = \begin{cases}
\frac{1}{6}(G(x,\beta,z-\delta)+G(x,\beta,z+\delta)+4G(x,\beta,z)) & \text{if} & -0.8 \leq x < -0.6, \\
1 & \text{if} & -0.4 \leq x < -0.2, \\
1 - |10(x-0.1)| & \text{if} & 0.0 \leq x < 0.2, \\
\frac{1}{6}(F(x,\alpha,a-\delta)+F(x,\alpha,a+\delta)+4F(x,\alpha,a)) & \text{if} & 0.4 \leq x < 0.6, \\
0 & & \text{otherwise,}
\end{cases} \tag{31}
$$

where

$$
G(x,\beta,z) = e^{-\beta(x-z)^2}, \tag{32}
$$

$$
F(x,\alpha,a) = \sqrt{\max(1-\alpha^2(x-a)^2,0)}, \tag{33}
$$

To compare the numerical accuracy, in addition to the L_1 and L_∞ errors, we also calculate the total error (E_{Total}), the dissipation error ($E_{Dissipation}$), and the dispersion error ($E_{Dispersion}$) [55] as follows

$$
E_{Total} = E_{Dissipation} + E_{Dispersion}, \tag{34}
$$

$$
E_{Dissipation} = \left(\sigma(u_i) - \sigma(u_i^e)\right)^2 + (\bar{u}_i - \bar{u}_i^e)^2, \tag{35}
$$

$$
E_{Dispersion} = 2(1-\rho)\sigma(\bar{u}_i)\sigma(u_i^e), \tag{36}
$$

where $\sigma(u_i)$ is the standard deviation of numerical solution u_i, and $\sigma(u_i^e)$ is the standard deviation of analytical solution u_i^e. $\bar{u}_i$, $\bar{u}_i^e$ are the mean values of u_i and u_i^e. ρ is the correlation coefficient of u_i and u_i^e, and it is defined as

$$
\rho = \frac{cov(u_i,u_i^e)}{\sigma(u_i)\sigma(u_i^e)}, \tag{37}
$$

where $cov(u_i,u_i^e)$ is the covariance of u_i and u_i^e.

Fig. 6 illustrates the numerical results of the WENO-JS, WENO-Z, MWENO-JS, MWENO-Z, BVD-WENOJS-THINC, BVD-WENOZ-THINC, BVD-MWENOJS-THINC, and BVD-MWENOZ-THINC schemes at t=2 (1 period).
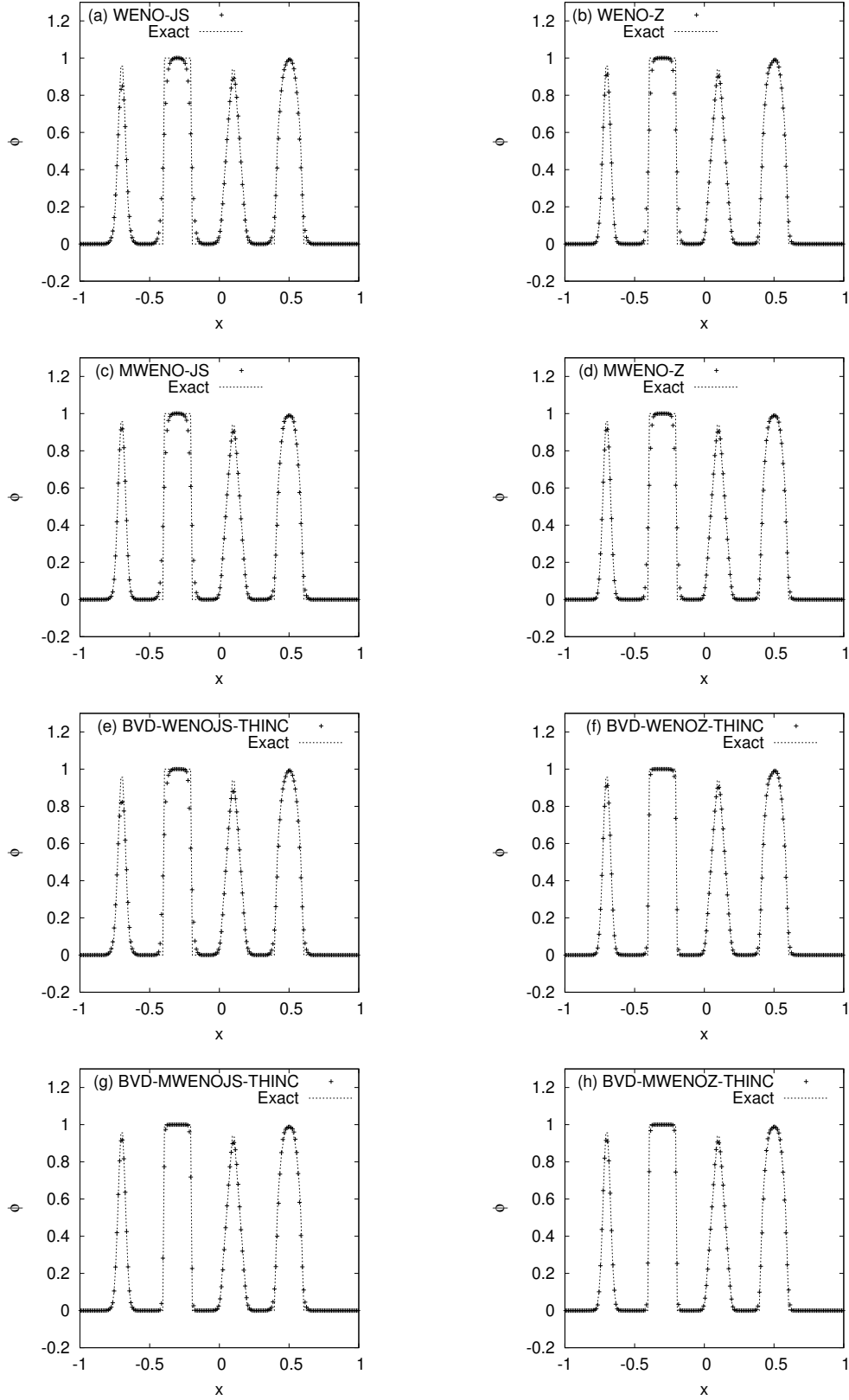
Figure 6: Numerical results of complex wave propagation test at t=2. N=200 and CFL=0.4 are used. (a) WENO-JS, (b) WENO-Z, (c) MWENO-JS, (d)MWENO-Z, (e) BVD-WENOJS-THINC, (f) BVD-WENOZ-THINC, (g) BVD-MWENOJS-THINC, (h) BVD-MWENOZ-THINC

It is observed that both BVD-WENOZ-THINC and BVD-MWENO-THINC perform better than WENO-Z and MWENO for discontinuities. In addition, BVD-MWENO-THINC obtains a sharper solutions for the cusps and the square profile than BVD-WENOZ-THINC. Table 3 presents the results of numerical errors of the WENO-Z,

Table 3: Errors in capturing the complex wave propagation test at t=2. N=200 and CFL=0.4 are used

	Total error	Dissipation error	Dispersion error	L_1 error	L_∞ error
WENO-JS	5.88×10^{-3}	6.45×10^{-4}	5.24×10^{-3}	3.12×10^{-2}	4.11×10^{-1}
WENO-Z	4.28×10^{-3}	2.47×10^{-4}	4.03×10^{-3}	2.23×10^{-2}	3.87×10^{-1}
MWENO-JS	4.73×10^{-3}	3.18×10^{-4}	4.42×10^{-3}	2.48×10^{-2}	3.81×10^{-1}
MWENO-Z	3.92×10^{-3}	1.70×10^{-4}	3.75×10^{-3}	2.05×10^{-2}	3.80×10^{-1}
BVD-WENOJS-THINC	4.82×10^{-3}	4.56×10^{-4}	4.36×10^{-3}	2.63×10^{-2}	4.26×10^{-1}
BVD-WENOZ-THINC	2.05×10^{-3}	1.01×10^{-4}	1.95×10^{-3}	1.59×10^{-2}	3.01×10^{-1}
BVD-MWENOJS-THINC	1.84×10^{-3}	7.91×10^{-5}	1.77×10^{-3}	1.54×10^{-2}	2.82×10^{-1}
BVD-MWENOZ-THINC	1.44×10^{-3}	6.70×10^{-5}	1.37×10^{-3}	1.38×10^{-2}	2.19×10^{-1}

MWENOZ, BVD-WENOZ-THINC, and BVD-MWENO-THINC schemes. The results reveal that MWENO has less numerical errors than WENO-Z. Both BVD-WENOZ-THINC and BVD-MWENO-THINC have smaller numerical errors compared to WENOZ and MWENO, respectively. Moreover, BVD-MWENOZ-THINC has the least numerical errors.

3.3.3. Extrema of the various smoothness problem

In this section, we verify the proposed scheme by capturing the extrema of the various smoothness test, and the initial condition is given as

$$\phi(x+0.5,0) = \begin{cases} -x\sin(1.5\pi x^2) & \text{if} & -1 \le x < -1/3 \\ |\sin(2\pi x)| & \text{if} & |x| \le 1/3 \\ 2x - 1 - \sin(3\pi x)/6 & \text{otherwise,} \end{cases} \tag{38}$$

for $-1 \le x \le 1$. $u(x) = 1$, $N = 100$, CFL $= 0.4$ and periodic boundary conditions are used. Numerical results at $t = 2$ (1 period) are shown in Fig. 7. It is evident that BVD-WENOZ-THINC performs better than WENO-Z and MWENO for discontinuities. In addition, BVD-MWENO-THINC obtains a sharper solution for discontinuities than BVD-WENOZ-THINC.
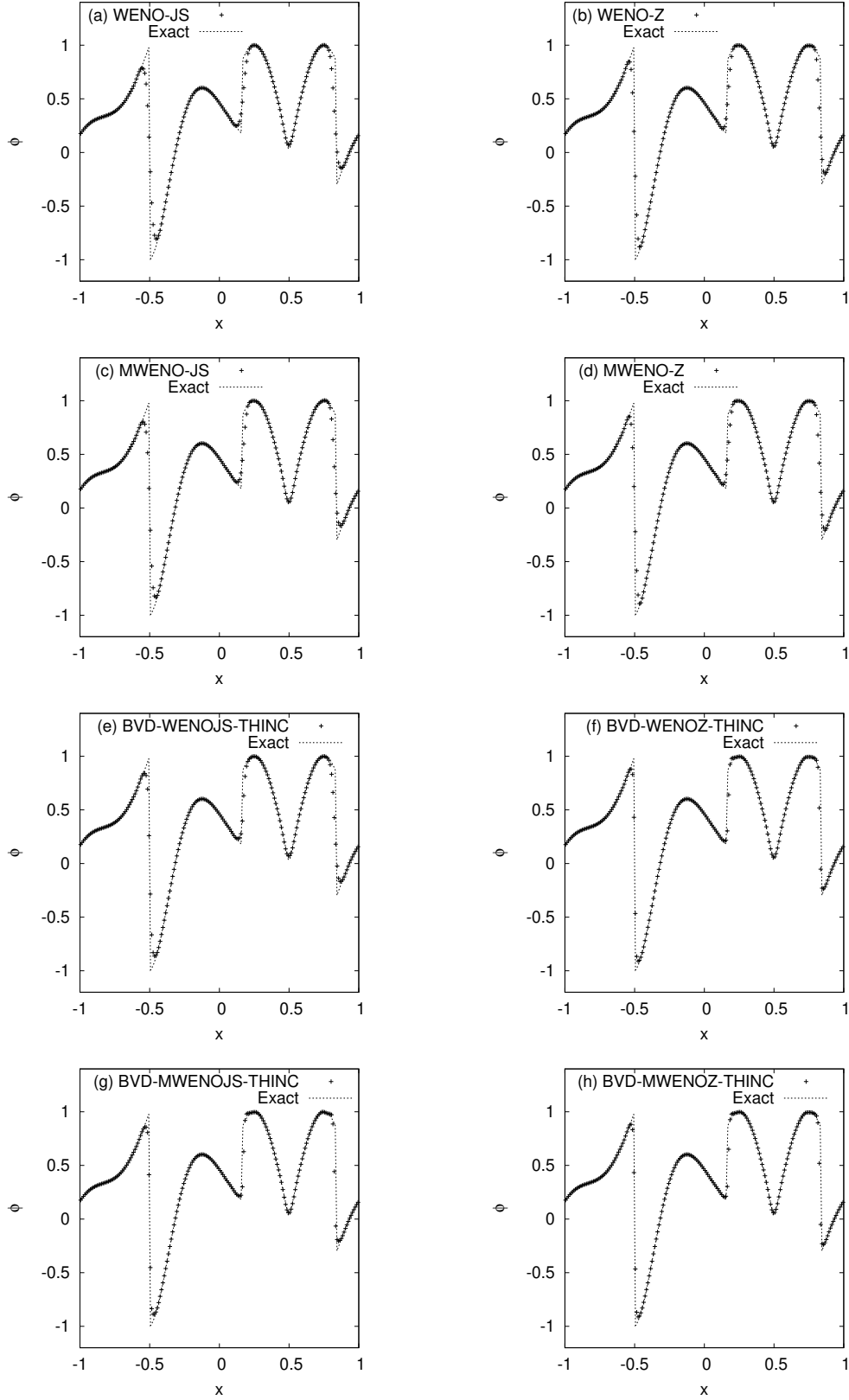
Figure 7: Numerical results of capturing the extrema of the various smoothness test at t=2. N=200 and CFL=0.4 are used. (a) WENO-JS, (b) WENO-Z, (c) MWENO-JS, (d)MWENO-Z, (e) BVD-WENOJS-THINC, (f) BVD-WENOZ-THINC, (g) BVD-MWENOJS-THINC, (h) BVD-MWENOZ-THINC

Table 4: Numerical errors in the capturing extrema of the various smoothness test at t=2. N=100 and CFL=0.4 are used

	Total error	Dissipation error	Dispersion error	L_1 error	L_∞ error
WENO-JS	1.55×10^{-2}	1.92×10^{-3}	1.36×10^{-2}	3.71×10^{-2}	8.39×10^{-1}
WENO-Z	1.17×10^{-2}	1.00×10^{-3}	1.07×10^{-2}	2.77×10^{-2}	7.87×10^{-1}
MWENO-JS	1.30×10^{-2}	1.41×10^{-3}	1.16×10^{-2}	3.16×10^{-2}	7.99×10^{-1}
MWENO-Z	1.16×10^{-2}	9.50×10^{-3}	1.06×10^{-2}	2.75×10^{-2}	7.83×10^{-1}
BVD-WENOJS-THINC	9.99×10^{-3}	9.71×10^{-4}	9.02×10^{-3}	2.64×10^{-2}	7.22×10^{-1}
BVD-WENOZ-THINC	4.69×10^{-3}	2.96×10^{-4}	4.39×10^{-3}	1.49×10^{-2}	5.83×10^{-1}
BVD-MWENOJS-THINC	5.21×10^{-3}	3.55×10^{-4}	4.86×10^{-2}	1.66×10^{-2}	5.69×10^{-1}
BVD-MWENOZ-THINC	4.54×10^{-3}	2.66×10^{-4}	4.28×10^{-3}	1.46×10^{-2}	5.49×10^{-1}

Table 4 shows the results of numerical errors of the WENO-Z, MWENO, BVD-WENOZ-THINC, and BVD-MWENO-THINC schemes. Results show that MWENO has less numerical errors than WENO-Z. BVD-WENOZ-THINC and BVD-MWENO-THINC can reduce numerical errors from WENOZ and MWENO effectively. Overall, BVD-MWENOZ-THINC has the least numerical errors. The results are consistent with the results of the complex wave propagation test.

3.4. Euler equation

In this section, we validate the proposed schemes by solving the Euler equations of gas dynamics. The numerical results of the proposed MWENO-Z and BVD-MWENOZ-THINC schemes are compared to the results of the WENO-Z[6] and BVD-WENOZ-THINC [54] schemes.

3.4.1. Sod's problem

Sod's problem [53] is one of the most widely used benchmark tests for one-dimensional Euler equations. The initial condition is given as follows

$$
\begin{aligned}
\rho(x,0) &= 1; & u(x,0) &= 0; & p(x,0) &= 1; & \text{if } x < 0.5 \\
\rho(x,0) &= 0.125; & u(x,0) &= 0; & p(x,0) &= 0.1; & \text{otherwise,}
\end{aligned}
\tag{39}
$$

where ρ is density and p is pressure. We carry out the numerical simulation with the mesh size $N = 100$ until time at $t = 0.2$. Fig. 8 shows the numerical results of density. It is observed that WENO-Z, MWENO-Z, BVD-WENOZ-THINC, and BVD-MWENOZ-THINC capture contact discontinuity and shock well without oscillation. In terms of the discontinuity region, BVD-WENOZ-THINC and BVD-TWENOZ-THINC resolve the discontinuity with less numerical dissipation than WENO-Z and MWENO-Z.
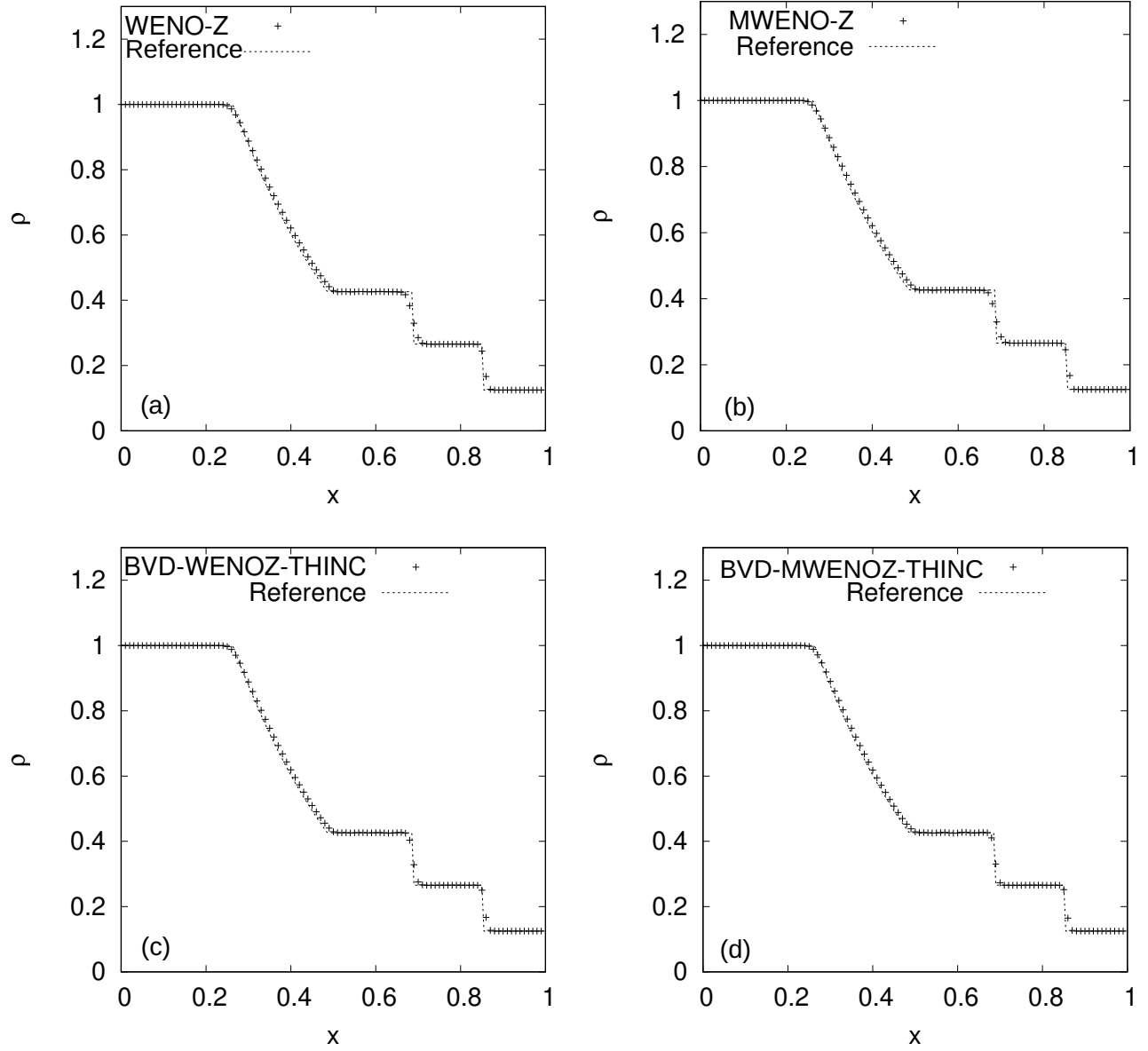
Figure 8: Numerical results for Sod's shock tube problem at t = 0.2 with density output (CFL=0.2 and N=100). (a) WENO-Z, (b) MWENO-Z, (c) BVD-WENOZ-THINC, (d) BVD-MWENOZ-THINC

3.4.2. Lax's problem

In Lax's problem[61], the numerical test with strong shock and contact discontinuity is characterized by the following initial condition

$$\rho(x,0) = 0.445; \quad u(x,0) = 0.698; \quad p(x,0) = 3.528; \quad \text{if } x < 0.5,$$
$$\rho(x,0) = 0.5; \quad\quad u(x,0) = 0; \quad\quad\quad p(x,0) = 0.571; \quad \text{otherwise.}$$

(40)

It is observed that WENO-Z, MWENO-Z, BVD-WENOZ-THINC and BVD-MWENOZ-THINC capture shocks well
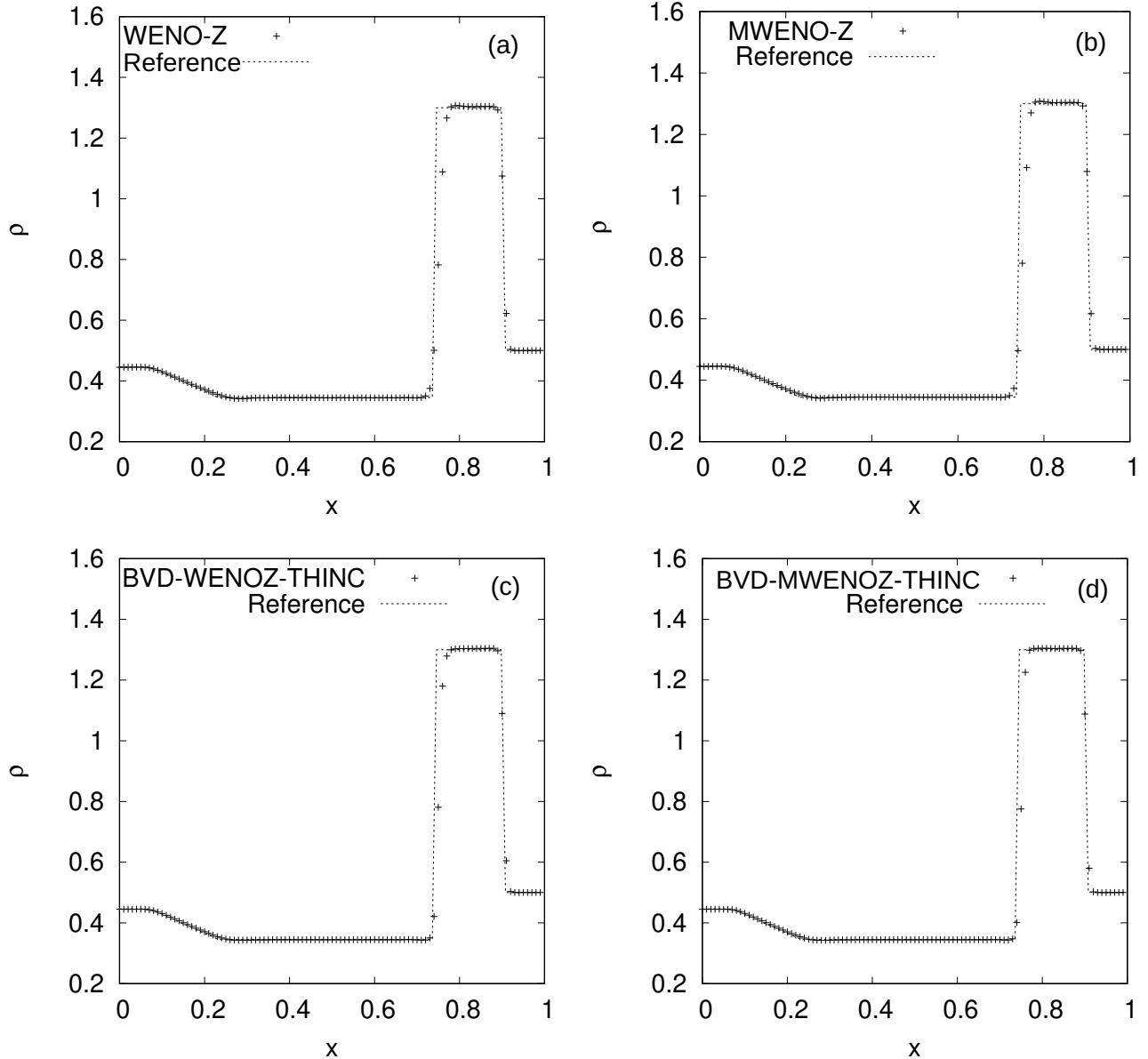
Figure 9: Numerical results of Lax's shock tube problem at t=0.16 (CFL=0.2 and N=100).(a) WENO-Z, (b) MWENO-Z, (c) BVD-WENOZ-THINC, (d) BVD-MWENOZ-THINC

without numerical oscillation. BVD-WENOZ-THINC performs better than WENO-Z for capturing discontinuity. In

addition, BVD-MWENOZ-THINC resolves the discontinuity with less numerical dissipation than BVD-WENOZ-THINC. This observation is consistent with the results of Sod's problem.

3.4.3. Shock turbulence problem

This test is used to solve the shock-turbulence problem [49] with discontinuities, low-frequency and high-frequency wave profiles. Interactions between a shock wave and perturbations are simulated with the following initial condition

$$
\begin{aligned}
&\rho(x,0) = 3.857148; && u(x,0) = 2.629369; && p(x,0) = 10.333333; && \text{if } 0 \leq x < 1 \\
&\rho(x,0) = 1 + 0.2\sin(50x - 25); && u(x,0) = 0; && p(x,0) = 1; && \text{otherwise.}
\end{aligned}
\tag{41}
$$
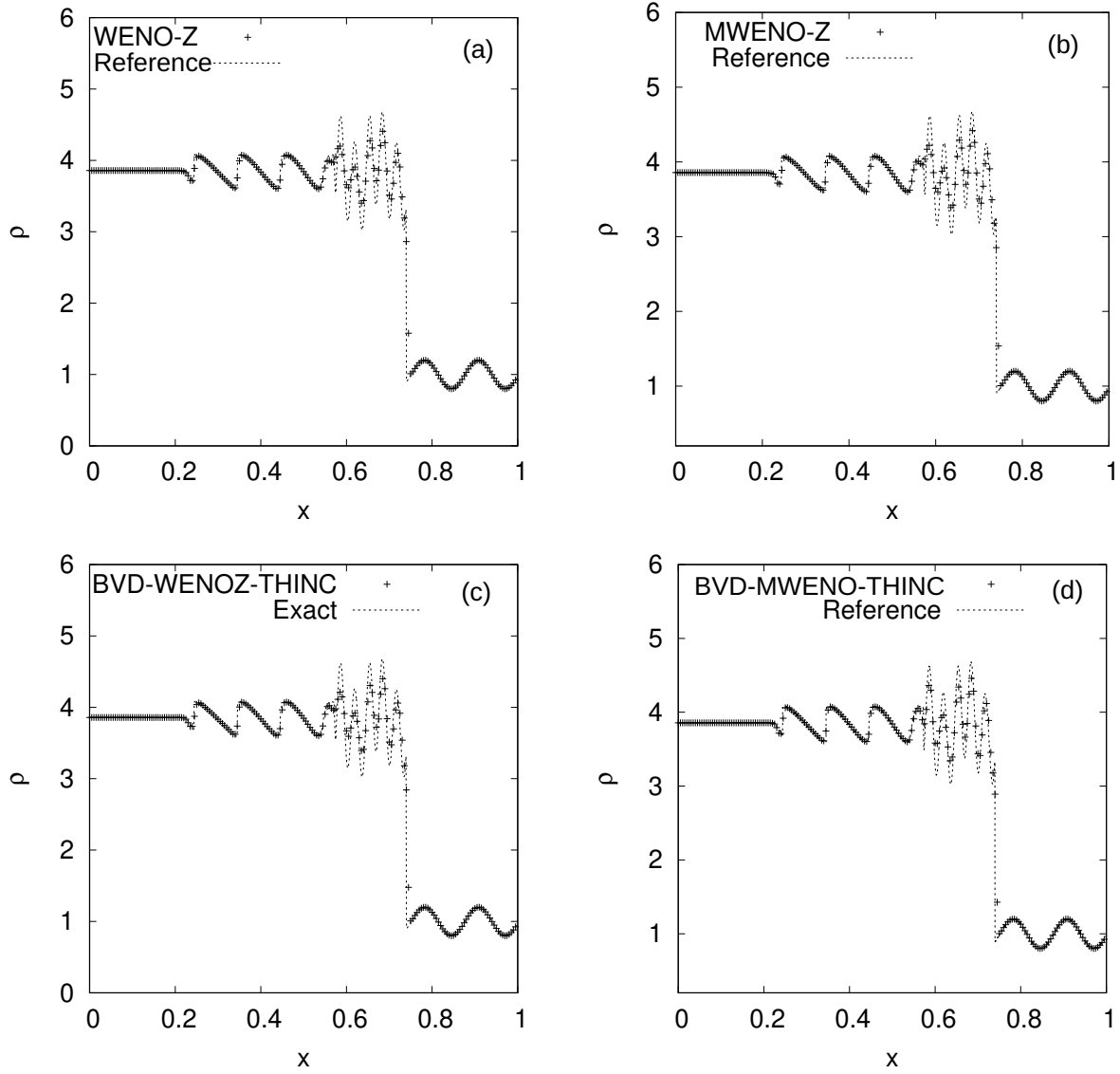
Figure 10: Numerical results of shock-turbulence interaction problem at time t=1.8 (CFL=0.2 and N=200). (a) WENO-Z, (b) MWENO-Z, (c) BVD-WENOZ-THINC, (d) BVD-MWENOZ-THINC

Fig. 10 shows the numerical results of WENO-Z, MWENO-Z, BVD-WENOZ-THINC and BVD-TWENOZ-THINC at t=1.8. It is observed that there is no significant difference for capturing low-frequency wave profiles among all the compared schemes. However, for high-frequency wave profiles, BVD-MWENOZ-THINC outperforms WENO-Z, MWENO-Z and BVD-WENOZ-THINC.

3.4.4. Another shock turbulence problem

Another shock density wave interaction test is conducted to show the high resolution property of the new proposed scheme. Interactions between a shock wave and perturbations are simulated with the following initial condition

$$\begin{aligned}
&\rho(x,0) = 1.515695; &&u(x,0) = 0.523346; &&p(x,0) = 1.805; &&\text{if } xle-4.5 \\
&\rho(x,0) = 1+0.1sin(10\pi x); &&u(x,0) = 0; &&p(x,0) = 1; &&\text{otherwise.}
\end{aligned} \tag{42}$$
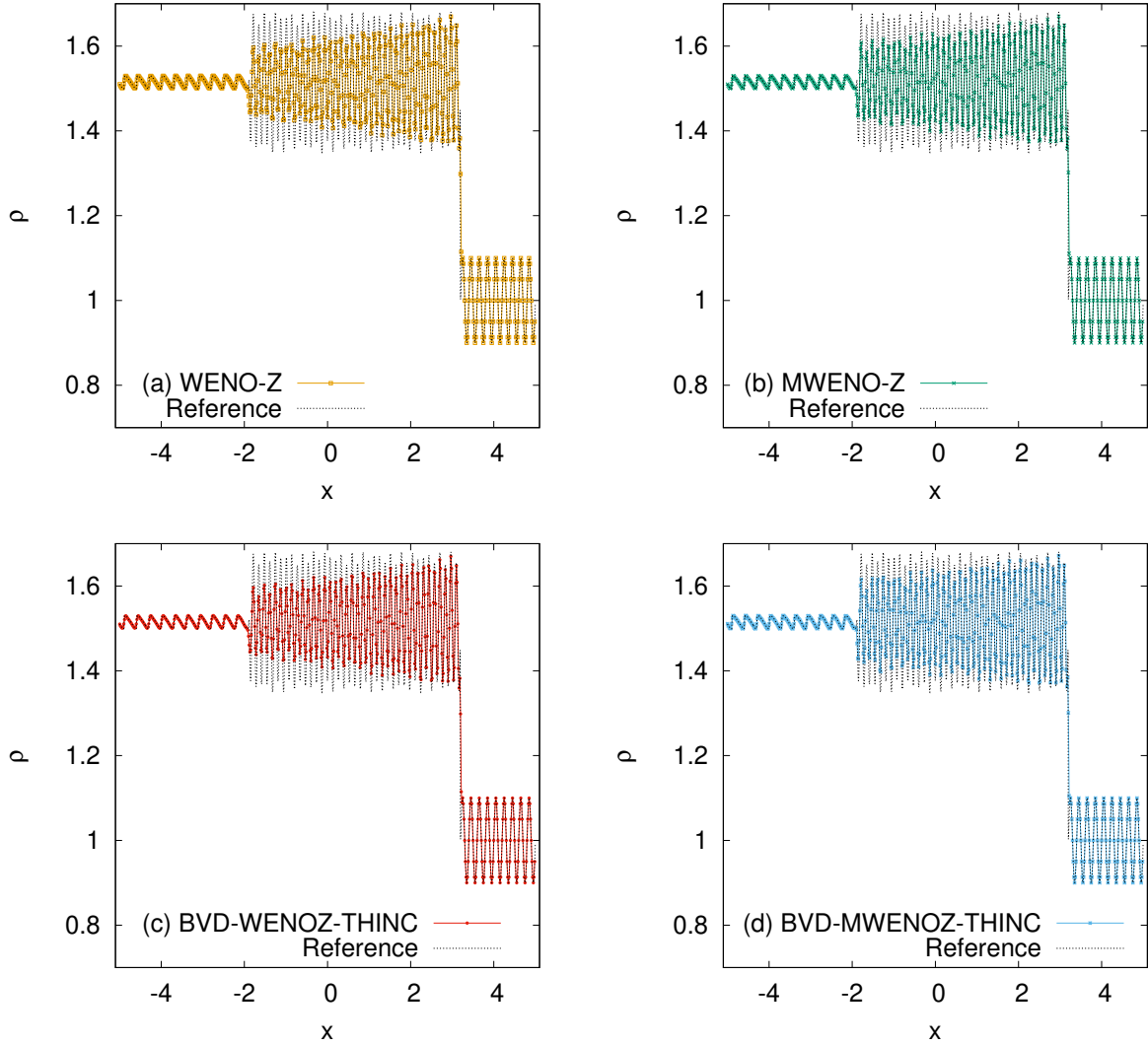
Figure 11: Numerical results of shock-turbulence interaction problem by using WENO-Z, MWENO-Z, BVD-WENOZ-THINC, and BVD-MWENOZ-THINC at time t=5.0 (CFL=0.2 and N=600).
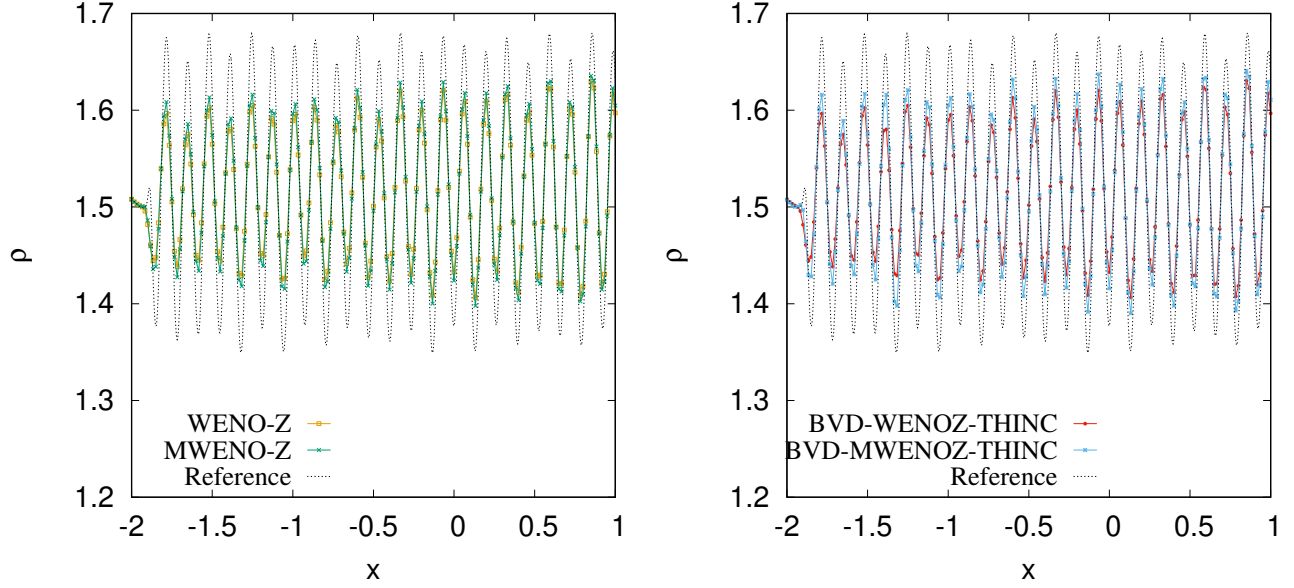
Figure 12: Amplified view of numerical results of shock-turbulence interaction problem by using WENO-Z, MWENO-Z, BVD-WENOZ-THINC, and BVD-TWENOZ-THINC at time t=5.0 (CFL=0.2 and N=600).

Fig. 11 shows the numerical results of WENO-Z, MWENO-Z, BVD-WENOZ-THINC, and BVD-TWENOZ-THINC at t=5.0 and Fig. 12 shows a zoomed region for density perturbation. It is observed that the flow structure is smeared out by using WENO-Z and BVD-WENOZ-THINC, while MWENO-Z and BVD-MWENOZ-THINC performs better than WENO-Z and BVD-WENOZ-THINC, respectively. Moreover, BVD-TWENOZ-THINC show the best solution performance in maintaining the amplitudes of density waves. This indicates that the proposed scheme has a high resolution property enabling it to better solve complex flow sturctures especially for shock-turbulence interaction problems.

3.4.5. Two blast waves interaction problem

We also validate the proposed schemes through two interacting blast waves test [62] with the following initial conditions

$$(\rho_0, u_0, p_0) = \begin{cases} (1, 0, 1000) & \text{for} \quad 0 \leq x < 0.1, \\ (1, 0, 0.01) & \text{for} \quad 0.1 \leq x <= 0.9, \\ (1, 0, 100) & \text{otherwise.} \end{cases} \tag{43}$$

The numerical mesh size $N = 400$, and the reflecting boundary condition is used. In this test, two blast waves are formed by the initial jumps. Expansion fans, contact discontinuities, and strong shocks are generated and interact with each other. Due to the violent interaction, the existence of oscillation may cause the break up of the simulation. Another difficulty for existing shock-capturing schemes is the overly smeared density discontinuities in the numerical solution [54]. The results of WENO-Z, MWENO-Z, BVD-WENOZ-THINC, and BVD-MWENOZ-THINC at time $t = 0.038$ are shown in Fig. 13.
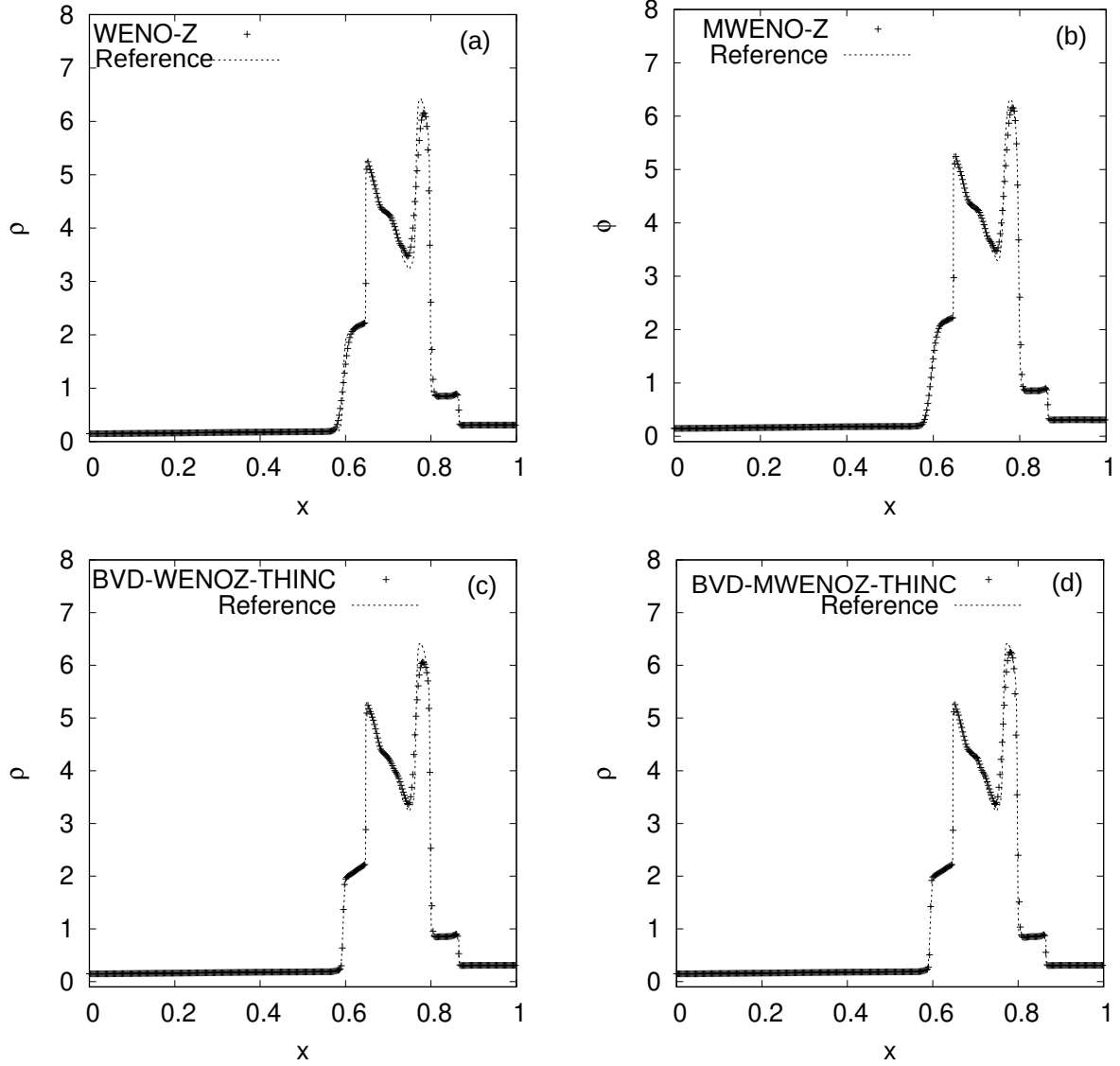
22

Figure 13: Numerical results of two interacting blasting waves problem at t=0.038 and N=400. (a) WENO-Z, (b) MWENO-Z, (c) BVD-WENOZ-THINC, (d) BVD-MWENOZ-THINC

It is observed that the left-most density discontinuity is smeared in the numerical solution of WENO-Z and MWENO-Z performs better than WENO-Z. Both BVD-WENOZ-THINC and BVD-MWENOZ-THINC reduce the numerical dissipation in the vicinity of the density discontinuity effectively. Compared to BVD-WENOZ-THINC, BVD-MWENOZ-THINC resolves the discontinuity with less numerical dissipation. In terms of capturing the shock, BVD-MWENOZ-THINC performs better than the BVD-WENOZ-THINC scheme. The resolution of the left-most density discontinuity by BVD-MWENOZ-THINC is superior to other existing shock capturing schemes without artificial compression steepening treatment.

3.4.6. 2D Double-Mach reflection problem

To verify the proposed method in capturing strong shocks and vortex, the Double-Mach reflection test [62] is conducted in this section.This benchmark test involves a Mach 10 shock hitting a ramp which is inclined by 30 degrees in a perfect gas. For simplicity, the coordinate system is aligned with the ramp for the numerical tests. Reflecting boundary condition is used on the bottom and an isolated moving oblique Mach 10 shock is imposed on the top. Inflow and outflow boundary conditions are used on the left and right sides. Fig. 14 shows the sketch of Double-Mach reflection problem, and Fig. 15 shows the experiment results performed by Smith [51].
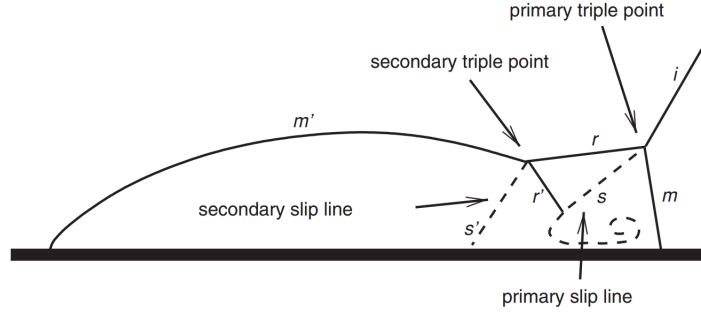
Figure 14: Sketch of Double-Mach reflection problem [31]
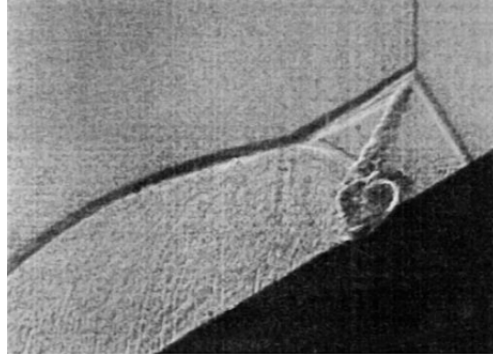
Figure 15: Experiment results of Double-Mach reflection problem performed by L.G. Smith [51]

In the Double-Mach problem, when the shock runs up the ramp, a self-similar shock structure with two triple points evolves, as shown in Fig. 14 [31]. At the primary triple point, the Mach stem (m), the incident shock (i), and the reflected shock (r) are joined. The reflected wave emanates from the triple point and travels transversely behind the incident shock. When the reflected shock r breaks up, a secondary triple point is formed. At the secondary triple point, the secondary mach stem (m'), the secondary reflected shock (r'), and the reflected shock r meet. From the primary triple point, a slip line (s) (sometimes called contact surface) emanates. The secondary reflected shock r' hits this slip line s and causes a curled flow structure, the resolution of which may serve as an indicator for the resolution of a numerical scheme [31].
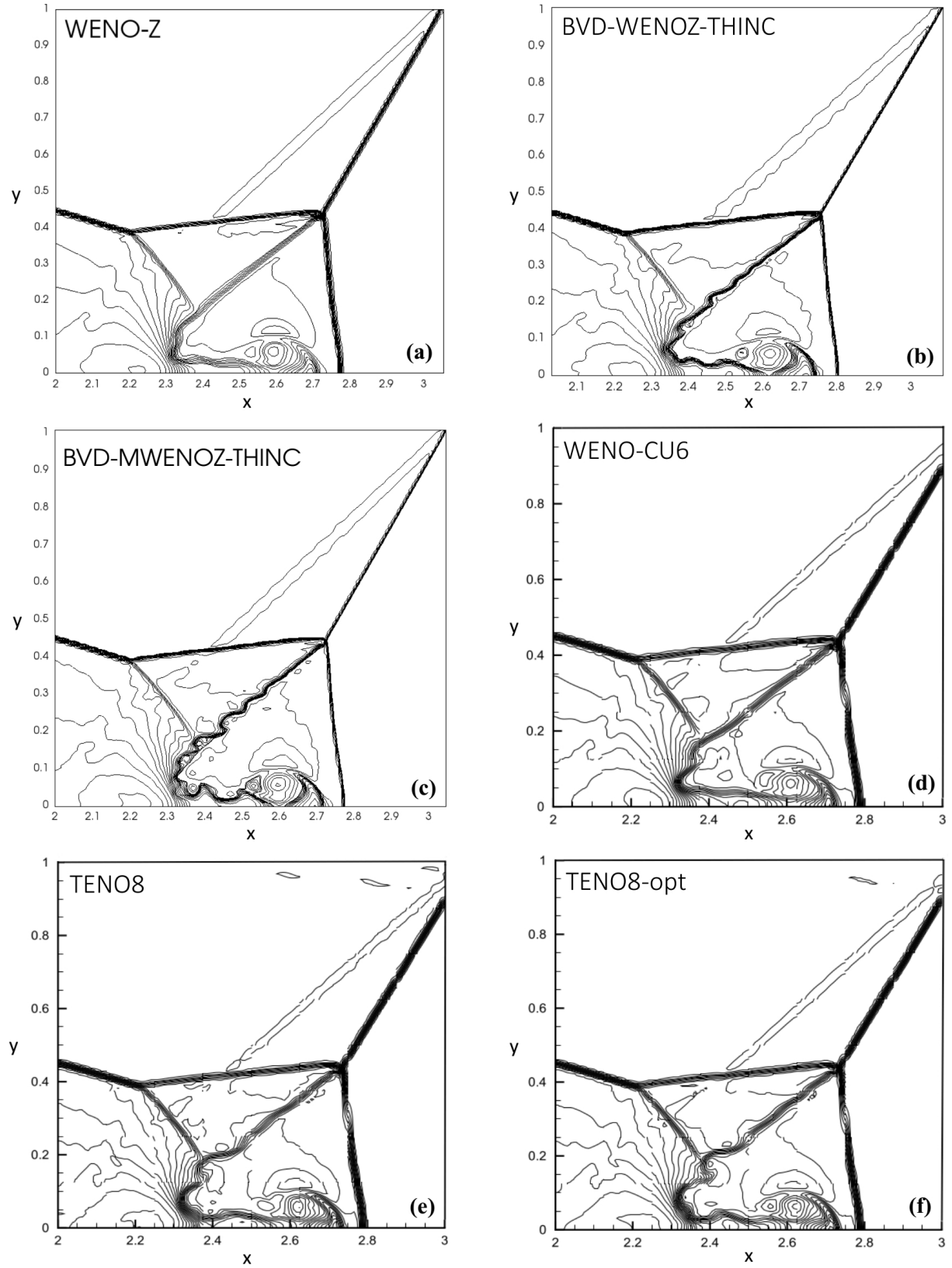
Figure 16: Numerical results of Double Mach reflection test by (a) WENO-Z, (b) BVD-WENOZ-THINC, (c) BVD-MWENOZ-THINC, (d) WENO-CU6, (e) TENO8, (f) TENO8-opt at t = 0.2 with meshes 512×128

25

Fig. 16 illustrates the numerical results of WENO-Z, BVD-WENOZ-THINC, and BVD-MWENOZ-THINC schemes up to $t = 0.2$ in the mesh of 512×128. In order to show more details of the vortical structure region, the zoomed-in view results are displayed with density contours between 1.887 and 20.9. In Fig. 16, the numerical results of WENO-Z, BVD-WENOZ-THINC, and BVD-MWENOZ-THINC schemes are also compared to the sixth-order WENOCU-6 [24] and eighth-order TENO8 and TENO8-opt schemes [14]. It is observed that BVD-MWENOZ-THINC captures the small-scale structures more clearly than WENO-Z and BVD-WENOZ-THINC. Moreover, BVD-MWENOZ-THINC also gets more clear high-resolution results for the vortical structures along the slip line compared to the results of the sixth-order WENOCU-6, eighth-order TENO8 and TENO8-opt schemes.

3.4.7. 2D shock-bubble interaction problem

In this section, we extend the BVD-MWENOZ-THIHC scheme to solve the five-equation model [1, 50] for compressible two-phase flow problems. The numerical model is formulated under a standard finite volume framework with a Riemann solver in the wave propagation form [32] and the BVD-MWENOZ-THINC scheme is applied to all state variables and volume fractions. Compressible two-phase flows contain a mixing region of two materials, the material interface of compressible two-phase flows makes the physics more complicate. When implementing the one-fluid model to compressible multiphase flow with moving interface, there are two substantial problems. Firstly, density and energy are calculated separately in addition to the indication function, hence special formulations are required to reach a balanced state among all variables for the interface cell. Secondly, the numerical dissipation in high-resolution schemes designed for solving single phase compressible flow involving shock waves tends to smear out discontinuities, including the material interfaces. To resolve the first issue, in this section, the five-equation model [3] is used as the Partial Differential Equation (PDE) that needs to be solved. This model combines Euler equations with interface indication function equations for each of fluid components, which is used as an efficient approximation to the state of the interface cell. To resolve the second issue, the proposed spatial reconstruction scheme BVD-MWENOZ-THINC is used to reduce numerical dissipation so as to maintain the sharpness of the jumps in volume fraction that identify the moving interfaces.

Shock-bubble interaction test is a compressible two-phase flow with moving interfaces problem. In the test, we investigate the interactions between a shock and a bubble, which involves the collision of a shock wave of Mach 1.22 in the air impacting a circular bubble gas. In the experiments performed by Haas et al. [19] and James et al. [43], a stationary cylindrical gas bubble is impacted by a leftward-moving Mach 1.22 planar shock wave in air. The bubbles were produced by inflating a cylindrical former whose walls were made from a very thin membrane of nitrocellulose. Good control was exercised over the shape of the bubble and the resultant flows were almost two-dimensional, thus the two-dimensional computational set-up can be expected to mimic the experiments fairly [43].
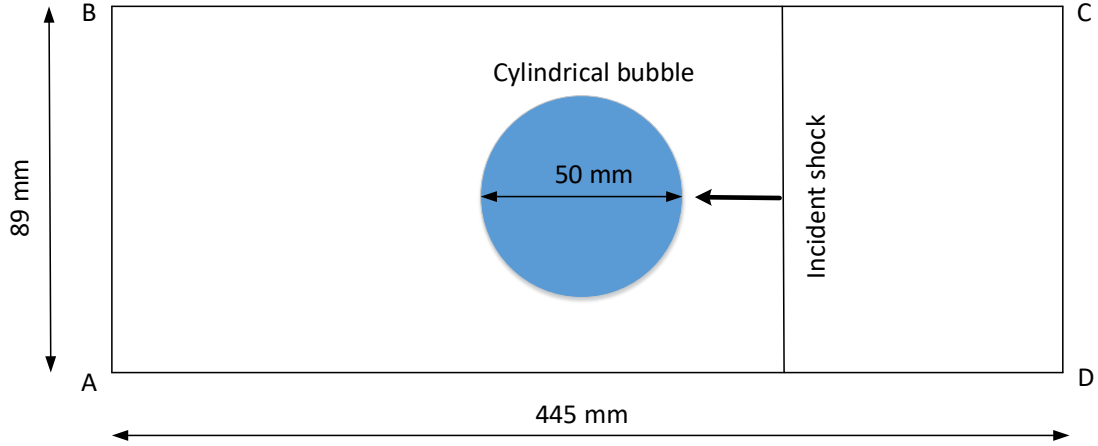
Figure 17: A schematic of the computational domain

The schematic of the computational set-up is shown in Fig. 17. The computation domain is $[0, 445] \times [0, 89] mm^2$. The radius of the bubble is $r_0 = 25$ mm, and the location of the shock is $x = 275$ mm. The domain is discretized by Cartesian grids with the mesh size $\Delta x = \Delta y = \frac{1}{4}$ mm, which represents a grid resolution of 400 cells across the bubble diameter. The symmetric-plane boundary conditions are used on the top and bottom, and the zero-gradient boundary conditions are used on the left and right. In the numerical test, both air and bubble are modelled as perfect gases. The initial state variables of 2D shock-bubble interaction test are shown in Table 5.

Table 5: The initial state quantities of 2D shock-bubble interaction problem. Inside the gas bubble (k=1), pre-shock regions outside the bubble (k=2), and post-shock regions outside the bubble (k=3)

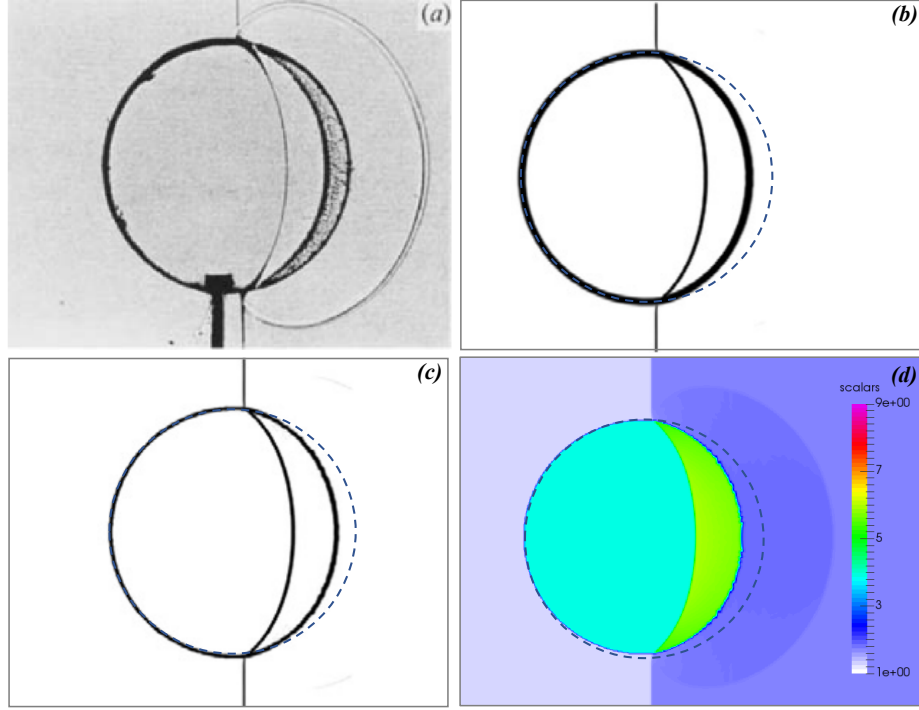| k	$\rho_1 (kg/m^3)$	$\rho_2 (kg/m^3)$	u (m/s)	v (m/s)	p (Pa)	α_1
1	3.863	1.225	0	0	1.01325×10^5	$1 - 10^{-8}$
2	3.863	1.225	0	0	1.01325×10^5	10^{-8}
3	3.863	1.686	113.5	0	1.59×10^5	$1 - 10^{-8}$

Figure 18: Results for a planar Mach 1.22 shock wave in air interacting with a circular R22 gas bubble at t = 55 μs. (*a*) experiment, (*b*) VOF, (*c*) VOF with interface-sharpening, and (*d*) BVD-MWENOZ-THINC
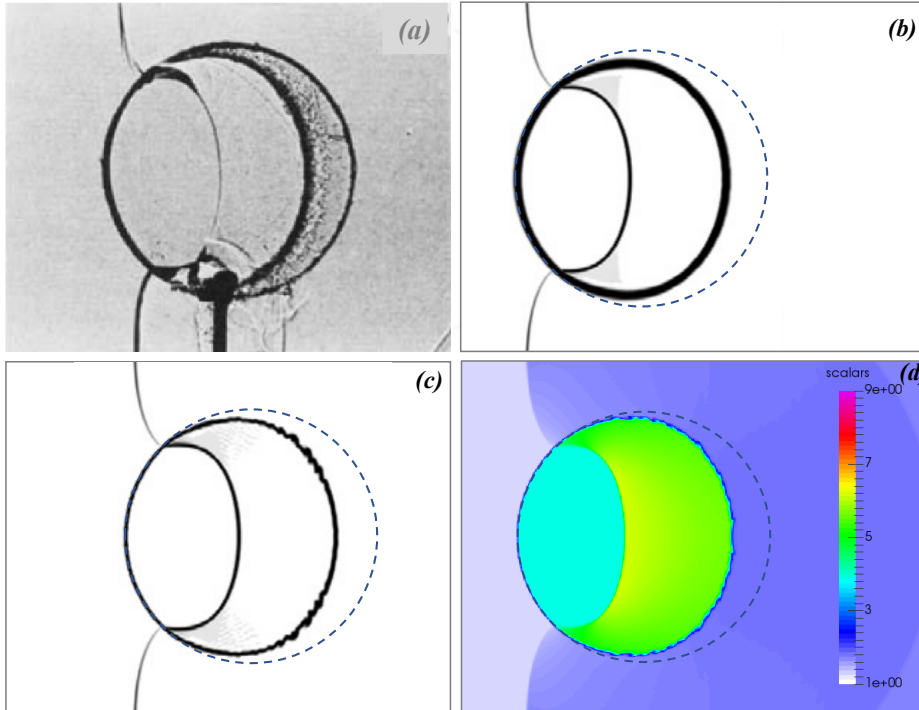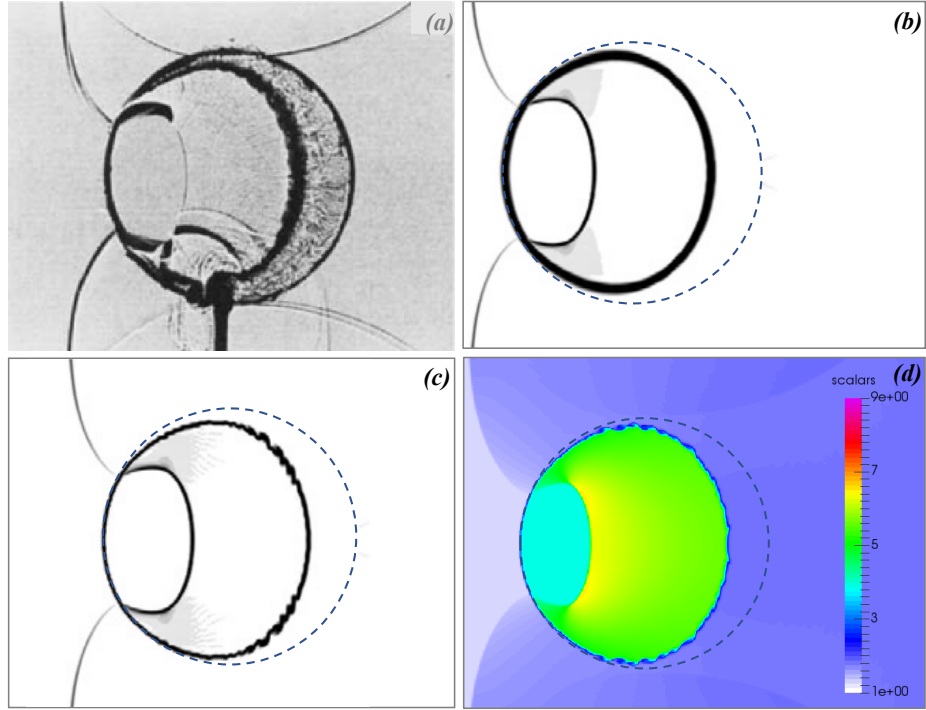

Figure 19: Same as Fig. 18, but at t = 115 μs
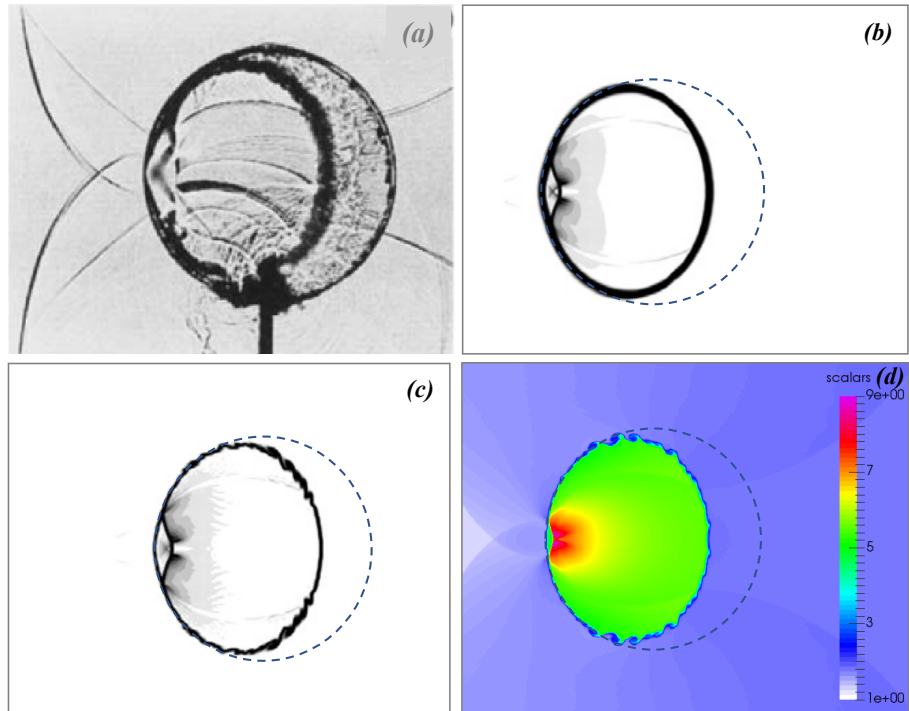
Figure 20: Same as Fig. 18, but at t = 135 μs
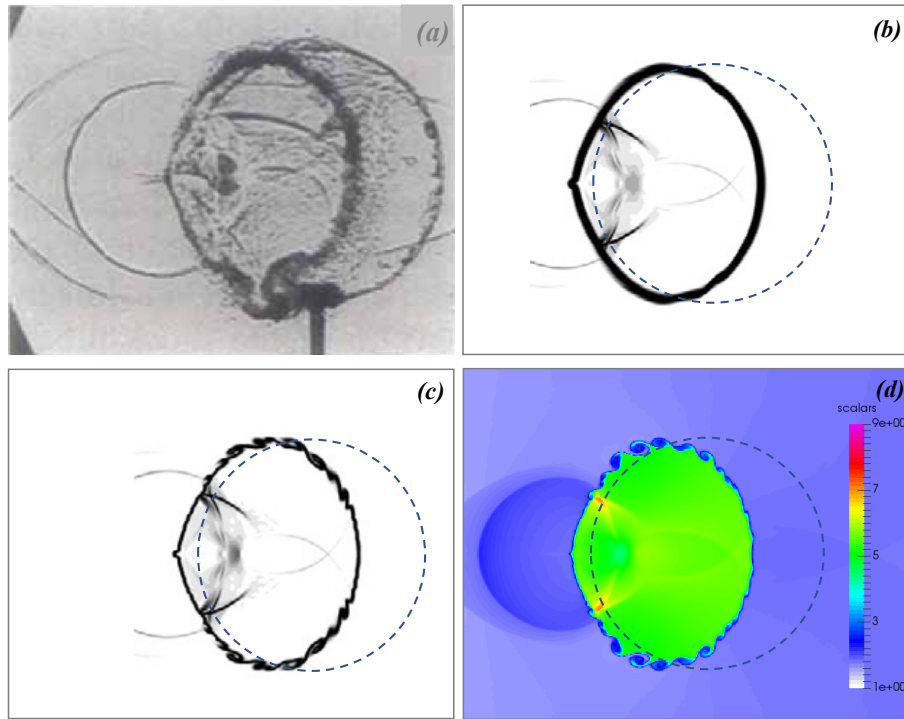

Figure 21: Same as Fig. 18, but at t = 187 μs
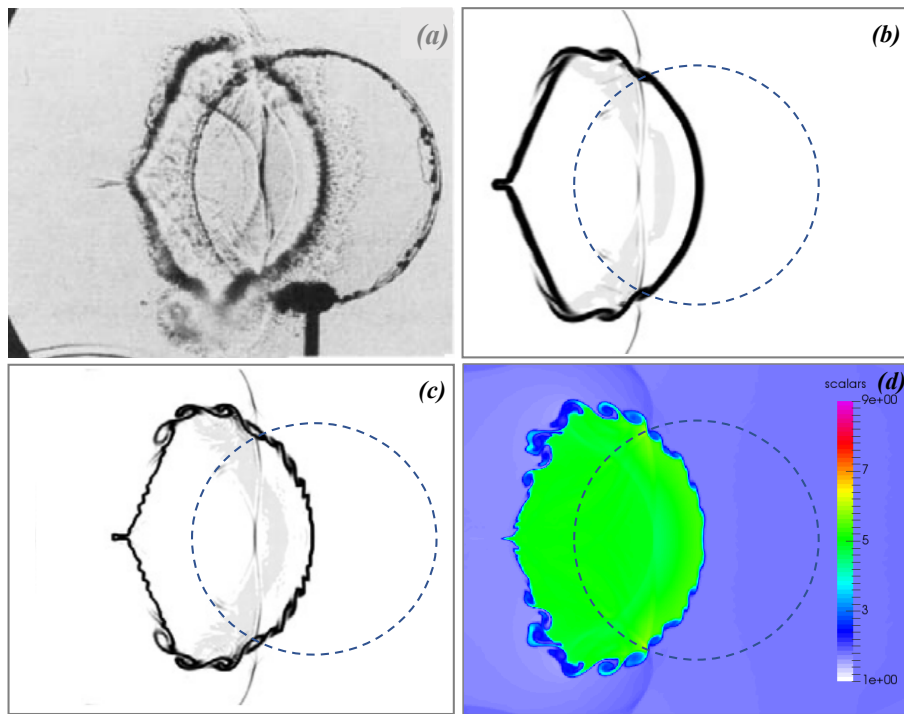
Figure 22: Same as Fig. 18, but at t = 247 μs
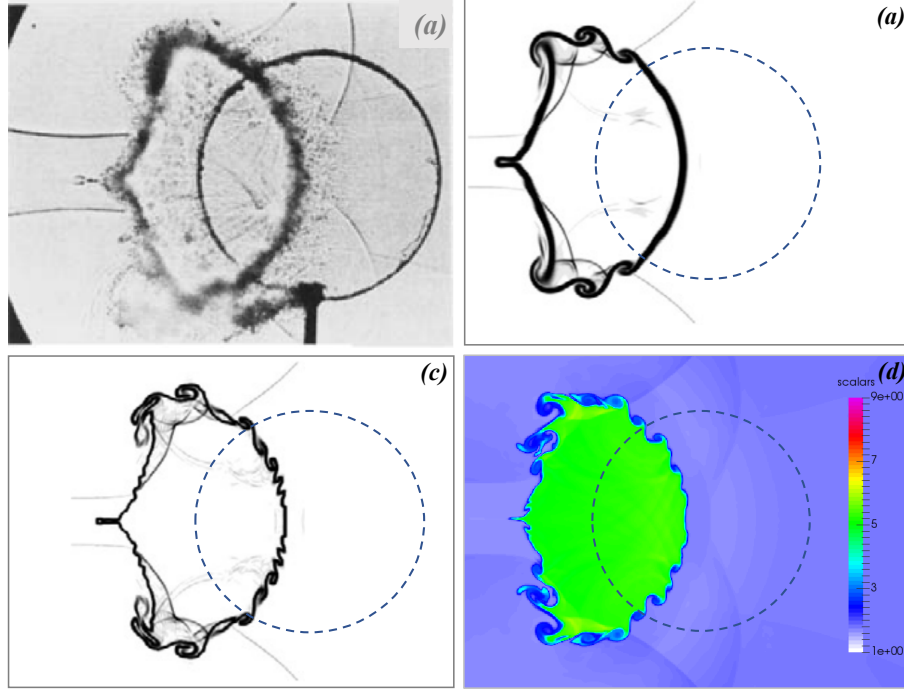

Figure 23: Same as Fig. 18, but at t = 342 μs

Figure 24: Same as Fig. 18, but at t = 417 μs

Figs. 18, 19, 20, 21, 22, 23, and 24 illustrate the results of the density at different times t = 55 μs, 115 μs, 135 μs, 187 μs, 247 μs, 342 μs, 417 μs by the BVD-MWENOZ-THINC scheme compared to the experimental results and previous numerical simulations by volume-of-fluid (VOF) methods (including the results with and without the application of anti-diffusion interface-sharpening) [52] on same grids. The circle in the experimental results represent the initial bubble frame, and the dash line circle in the numerical results represent the initial bubble profile.

In the early stage at t = 55 μs, the bubble experiences only large-scale deformations, so that no non-resolved scales are generated. The interface profile captured by numerical methods at this time agrees well with the experimental results. As time moves on, due to the vorticity induced by incident shock impact, the instability develops along with the interface, which begins to roll up and produces small filaments, as shown in Figs. 19, 20, 21, 22, 23, and 24. These fine structures tend to be smeared out by numerical schemes with large numerical dissipation unless high-resolution computational meshes are used [52]. It is observed that the BVD-MWENOZ-THINC scheme maintains the compact thickness of the material interfaces and gives large-scale flow structures similar with the results computed from the VOF method with the application of anti-diffusion interface-sharpening technique on the same grid resolution.

It should be noted that numerical simulation captures more small-scale vortical structures compared to experimental results. It is probably due to the absence of physical viscosity in the flow model. In the numerical simulation, which is inviscid, the vortices will be continuously enforced when refined grid resolution is used [36]. The significance of the TBVD-MWENOZ-THINC scheme with reduced numerical dissipation lies in the real-case applications. For instance, in molecular or turbulent mixing problems, physical dissipation plays an important role. The flow structures can be more faithfully reproduced by using high-resolution numerical scheme with reduced numerical dissipation.

4. Conclusions

In this paper, firstly, we proposed the modified WENO reconstruction strategy based on the fifth-order WENO scheme. Instead of using all adjacent smooth sub-stencils, the interpolation was built on two target adjacent sub-stencils or three target sub-stencils to optimize contributions of the polynomials over different candidate stencils and to recover the highest possible order in the vicinity of critical points. Secondly, an adaptive parameter was designed to control the jump thickness of the THINC scheme for multi-dimensional calculation. Based on the MWENO and THINC schemes, a high-resolution BVD-MWENOZ-THINC scheme was proposed by implementing a BVD selection algorithm. A number of numerical tests for both scalar cases, linear and nonlinear, and system case with the Euler equations of gas dynamics and compressible two-phase problem are carried out to validate the proposed scheme. The results reveal that the presented modification of fifth-order WENO reconstruction has been successfully applied to WENO-JS and WENO-Z schemes with improved solution and the adaptive beta can improve accuracy of multi-dimensional calculation. It is also found that the proposed BVD-MWENOZ-THINC scheme has fifth-order accuracy for smooth solutions. Meanwhile, the BVD-MWENOZ-THINC scheme can capture both smooth and discontinuous solutions simultaneously with less numerical errors compared to the WENO-Z and BVD-WENOZ-THINC schemes. Moreover, the numerical results of the 2D double Mach reflection tests have shown that the resolution of the BVD-MWENOZ-THINC scheme is superior to the WENO-Z, BVD-WENOZ-THINC, WENO-CU6, TENO8 and TENO8-opt schemes with the same mesh of 512×128. This indicates that the BVD-TWENOZ-THINC scheme can be an effective high-resolution numerical scheme to simulate compressible flow problems. In addition, the BVD-MWENOZ-THINC scheme was applied to solve the five-equation model for compressible two-phase flow problems. Numerical results of 2D Shock-bubble interaction problem have shown that the BVD-MWENOZ-THINC scheme reproduces the complex flow features with less numerical dissipation. This suggests that the BVD-MWENOZ-THINC scheme can be an effective and practical approach to be applied in the simulation of compressible two-phase flow problems where the physical dissipation plays an important role.

Data availability

The data that support the findings of this study are available from the corresponding author upon reasonable request.

References

[1] R. Abgrall and S. Karni. Computations of compressible multifluids. *Journal of computational physics*, 169(2):594–623, 2001.

[2] B. Ahmadi Befrui, A. Gosman, R. Issa, and A. Watkins. An implicit non-iterative solution procedure for the calculation of flows in reciprocating engine chambers. *Computer methods in applied mechanics and engineering*, 79(3):249–279, 1990.

[3] G. Allaire, S. Clerc, and S. Kokh. A five-equation model for the simulation of interfaces between compressible fluids. *Journal of Computational Physics*, 181(2):577–616, 2002.

[4] J. R. Blake and D. Gibson. Cavitation bubbles near boundaries. *Annual review of fluid mechanics*, 19(1):99–123, 1987.

[5] D. Bogdanoff. Compressibility effects in turbulent shear layers. *AIAA journal*, 21(6):926–927, 1983.

[6] R. Borges, M. Carmona, B. Costa, and W. S. Don. An improved weighted essentially non-oscillatory scheme for hyperbolic conservation laws. *Journal of Computational Physics*, 227(6):3191 – 3211, 2008.

[7] C. E. Brennen. *Cavitation and bubble dynamics*. Cambridge University Press, 2014.

[8] S. Chen, J. Wang, H. Li, M. Wan, and C. Shiyi. Spectra and mach number scaling in compressible homogeneous shear turbulence. *Physics of Fluids*, 30(065109), 2018.

[9] Z. Cheng, Y. Liu, M. Zhang, and J. Wang. Ib-weno method for incompressible flow with elastic boundaries. *Journal of Computational and Applied Mathematics*, 2018.

[10] B. Costa and W. S. Don. High order hybrid centralweno finite difference scheme for conservation laws. *Journal of Computational and Applied Mathematics*, 204(2):209 – 218, 2007. Special Issue: The Seventh International Conference on Mathematical and Numerical Aspects of Waves (WAVES05).

[11] R. N. Dahms and J. C. Oefelein. On the transition between two-phase and single-phase interface dynamics in multicomponent fluids at supercritical pressures. *Physics of Fluids*, 25(092103), 2013.

[12] X. Deng, Y. Shimizu, and F. Xiao. A fifth-order shock capturing scheme with two-stage boundary variation diminishing algorithm. *Journal of Computational Physics*, 386:323 – 349, 2019.

[13] P. F. Dunn, F. O. Thomas, M. P. Davis, and D. I. E. Experimental characterization of aviation-fuel cavitation. *Physics of Fluids*, 21(113302), 2009.

[14] L. Fu, X. Y. Hu, and N. A. Adams. A family of high-order targeted eno schemes for compressible-fluid simulations. *Journal of Computational Physics*, 305:333 – 359, 2016.

[15] T. B. Gatski and J. P. Bonnet. *Compressibility, turbulence and high speed flow*. Academic Press, 2013.

[16] L. Y. Gicquel, G. Staffelbach, and T. Poinsot. Large eddy simulations of gaseous flames in gas turbine combustion chambers. *Progress in Energy and Combustion Science*, 38(6):782–817, 2012.

[17] S. Gottlieb, C. W. Shu, and E. Tadmor. Strong stability-preserving high-order time discretization methods. *SIAM review*, 43(1):89–112, 2001.

[18] J. Guo and J. H. Jung. A numerical study of the local monotone polynomial edge detection for the hybrid weno method. *Journal of Computational and Applied Mathematics*, 321:232 – 245, 2017.

[19] J.-F. Haas and B. Sturtevant. Interaction of weak shock waves with cylindrical and spherical gas inhomogeneities. *Journal of Fluid Mechanics*, 181:4176, 1987.

[20] A. Harten, B. Engquist, S. Osher, and S. R. Chakravarthy. Uniformly high order accurate essentially non-oscillatory schemes, iii. *Journal of Computational Physics*, 131(1):3 – 47, 1997.

[21] D. C. Haworth and S. H. El Tahry. Probability density function approach for multidimensional turbulentflow calculations with application to in-cylinder flows in reciprocating engines. *AIAA journal*, 29(2):208–218, 1991.

[22] A. K. Henrick, T. D. Aslam, and J. M. Powers. Mapped weighted essentially non-oscillatory schemes: achieving optimal order near critical points. *Journal of Computational Physics*, 207(2):542–567, 2005.

[23] F. Hu, R. Wang, and X. Chen. A modified fifth-order wenoz method for hyperbolic conservation laws. *Journal of Computational and Applied Mathematics*, 303:56 – 68, 2016.

[24] X. Hu, Q. Wang, and N. A. Adams. An adaptive central-upwind weighted essentially non-oscillatory scheme. *Journal of Computational Physics*, 229(23):8952–8965, 2010.

[25] C. Huang and R. Wang. Mapped cweno scheme for hyperbolic conservation laws. *Journal of Computational and Applied Mathematics*, 344:229 – 244, 2018.

[26] M. Ida. Multibubble cavitation inception. *Physics of Fluids*, 21(113302), 2009.

[27] G. S. Jiang and C. W. Shu. Efficient implementation of weighted eno schemes. *Journal of Computational Physics*, 126(1):202 – 228, 1996.

[28] G.-S. Jiang and C.-W. Shu. Efficient implementation of weighted eno schemes. *Journal of computational physics*, 126(1):202–228, 1996.

[29] H. Jin, X. F. Liu, T. Lu, B. Cheng, J. Glimm, and D. H. Sharp. Rayleightaylor mixing rates for compressible flow. *Physics of Fluids*, 17(024104), 2005.

[30] C. Y. Jung and T. B. Nguyen. A new adaptive weighted essentially non-oscillatory weno- scheme for hyperbolic conservation laws. *Journal of Computational and Applied Mathematics*, 328:314 – 339, 2018.

[31] F. Kemm. On the proper setup of the double mach reflection as a test case for the resolution of gas dynamics codes. *Computers & Fluids*, 132:72 – 75, 2016.

[32] D. I. Ketcheson, M. Parsani, and R. J. LeVeque. High-order wave propagation algorithms for hyperbolic systems. *SIAM Journal on Scientific Computing*, 35(1):A351–A377, 2013.

[33] W. Kim, S. Menon, and H. C. Mongia. Large-eddy simulation of a gas turbine combustor flow. *Combustion Science and Technology*, 143(1-6):25–62, 1999.

[34] X. D. Liu, S. Osher, and T. Chan. Weighted essentially non-oscillatory schemes. *Journal of Computational Physics*, 115(1):200 – 212, 1994.

[35] Y. Lu, J. Katz, and A. Prosperetti. Dynamics of cavitation clouds within a high-intensity focused ultrasonic beam. *Physics of Fluids*, 25(073301), 2013.

[36] J. Luo, X. Hu, and N. A. Adams. Efficient formulation of scale separation for multi-scale modeling of interfacial flows. *Journal of Computational Physics*, 308:411–420, 2016.

[37] P. Moin and S. V. Apte. Large-eddy simulation of realistic gas turbine combustors. *AIAA journal*, 44(4):698–708, 2006.

[38] C. D. Ohl. Cavitation inception following shock wave passage. *Physics of Fluids*, 14(3512), 2002.

[39] S. Pirozzoli. On the spectral properties of shock-capturing schemes. *Journal of Computational Physics*, 219:489–497, 2006.

[40] M. S. Plesset and A. Prosperetti. Bubble dynamics and cavitation. *Annual review of fluid mechanics*, 9(1):145–185, 1977.

[41] D. H. Porter, A. Pouquet, and W. P. R. Inertial range structures in decaying compressible turbulent flows. *Physics of Fluids*, 10(237), 1998.

[42] J. Qiu. Weno schemes with laxwendroff type time discretizations for hamiltonjacobi equations. *Journal of Computational and Applied Mathematics*, 200(2):591 – 605, 2007.

[43] J. J. Quirk and S. Karni. On the dynamics of a shock–bubble interaction. *Journal of Fluid Mechanics*, 318:129–163, 1996.

[44] N. O. P. Raj and K. Venkatasubbaiah. A new approach for the design of hypersonic scramjet inlets. *Physics of Fluids*, 24(086103), 2012.

[45] A. M. Rogerson and E. Meiburg. A numerical study of the convergence properties of eno schemes. *Journal of Scientific Computing*, 5:151 – 167, 1990.

[46] H. I. Saravanamuttoo, G. F. C. Rogers, and H. Cohen. *Gas turbine theory*. Pearson Education, 2001.

[47] L. Selle, G. Lartigue, T. Poinsot, R. Koch, K. U. Schildmacher, W. Krebs, B. Prade, P. Kaufmann, and D. Veynante. Compressible large eddy simulation of turbulent combustion in complex geometry on unstructured meshes. *Combustion and Flame*, 137(4):489–505, 2004.

[48] Y. Shen and G. Zha. Improvement of weighted essentially non-oscillatory schemes near discontinuities. *Computers & Fluids*, 96:1–9, 2014.

[49] C. W. Shu and S. Osher. Efficient implementation of essentially non-oscillatory shock-capturing schemes. *Journal of Computational Physics*, 77(2):439 – 471, 1988.

[50] K.-M. Shyue. A fluid-mixture type algorithm for compressible multicomponent flow with mie–grüneisen equation of state. *Journal of Computational Physics*, 171(2):678–707, 2001.

[51] L. G. Smith. *Photographic investigations of the reflection of plane shocks in air*. 1945.

[52] K. So, X. Hu, and N. A. Adams. Anti-diffusion interface sharpening technique for two-phase compressible flow simulations. *Journal of Computational Physics*, 231(11):4304–4323, 2012.

[53] G. A. Sod. A survey of several finite difference methods for systems of nonlinear hyperbolic conservation laws. *Journal of computational physics*, 27(1):1–31, 1978.

[54] Z. Sun, S. Inaba, and F. Xiao. Boundary variation diminishing (bvd) reconstruction: A new approach to improve godunov schemes. *Journal of Computational Physics*, 322:309 – 325, 2016.

[55] L. L. Takacs. A two-step scheme for the advection equation with minimized dissipation and dispersion errors. *Monthly Weather Review*, 113(6):1050–1065, 1985.

[56] Y. Tian, W. Shi, F. Zhong, and J. Le. Pilot hydrogen enhanced combustion in an ethylene-fueled scramjet combustor at mach 4. *Physics of Fluids*, 33(015105), 2021.

[57] Y. Tomita. Jet atomization and cavitation induced by interactions between focused ultrasound and a water surface. *Physics of Fluids*, 26(097105), 2014.

[58] E. F. Toro. *Riemann solvers and numerical methods for fluid dynamics: a practical introduction*. Springer Science & Business Media, 2013.

[59] M. D. Turrell, P. J. Stopford, K. J. Syed, and E. Buchanan. Cfd simulation of the flow within and downstream of a high-swirl lean premixed gas turbine combustor. In *ASME Turbo Expo 2004: Power for Land, Sea, and Air*, pages 31–38. American Society of Mechanical Engineers, 2004.

[60] D. C. Venerus and D. J. Bugajsky. Compressible laminar flow in a channel. *Physics of Fluids*, 22(046101), 2010.

[61] P. Woodward and P. Colella. The numerical simulation of two-dimensional fluid flow with strong shocks. *Journal of computational physics*, 54(1):115–173, 1984.

[62] P. Woodward and P. Colella. The numerical simulation of two-dimensional fluid flow with strong shocks. *Journal of computational physics*, 54(1):115–173, 1984.

[63] F. Xiao, Y. Honma, and T. Kono. A simple algebraic interface capturing scheme using hyperbolic tangent function. *International Journal for Numerical Methods in Fluids*, 48(9):1023–1040, 2005.

[64] F. Xiao, S. Ii, and C. Chen. Revisit to the THINC scheme: a simple algebraic VOF algorithm. *Journal of Computational Physics*, 230(19):7086–7092, 2011.

[65] Y. Xing. High order finite volume weno schemes for the shallow water flows through channels with irregular geometry. *Journal of Computational and Applied Mathematics*, 299:229 – 244, 2016. Recent Advances in Numerical Methods for Systems of Partial Differential Equations.

[66] R. Zhang, M. Zhang, and C. Shu. High order positivity-preserving finite volume weno schemes for a hierarchical size-structured population model. *Journal of Computational and Applied Mathematics*, 236(5):937 – 949, 2011. The 7th International Conference on Scientific Computing and Applications, June 1316, 2010, Dalian, China.